coatings

Article

Laser Ablation of Copper Alloy under Varying Environmental Conditions to Achieve Purpose-Built Surface Structures

Asadullah Dawood [1,2,*], Naveed Ahmed [3,*], Shazia Bashir [1], Asma Hayat [1], Syed Muhammad Abouzar Sarfraz [4] and Ambreen Ayub [5]

1 Centre for Advanced Studies in Physics (CASP), Government College University, Lahore 54000, Pakistan
2 Department of Physics, National Excellence Institute University, Islamabad 04524, Pakistan
3 Department of Industrial Engineering, College of Engineering and Architecture, Al Yamamah University, Riyadh 11512, Saudi Arabia
4 Dipartimento Interateneo di Fisica, Università degli studi di Bari Aldo Moro, I-70126 Bari, Italy
5 Department of Physics, Women University Swabi, Swabi 23430, Pakistan
* Correspondence: asaddawood@gmail.com (A.D.); n_ahmed@yu.edu.sa (N.A.); Tel.: +92-332-4234070 (A.D.); +92-336-4647741 (N.A.)

Abstract: In the manufacturing industry, surface structures and surface topographies present at functional areas of the mechanical parts play a vital role in various performance characteristics, such as corrosion resistance, weldability, and wear behaviors, etc. Copper–zinc alloys are extensively used in the manufacturing industry. Laser ablation has the potential to create a variety of surface structures on the ablated substrate. The size and geometry of such structures largely depend on the selection of process parameters and the ablation environment. In the present study, a copper–zinc alloy (95% Cu and 5% Zn) has been laser ablated under different gaseous and magnetic environments to realize a variety of micro-structuring at the ablation surfaces. The effect of plasma plume pressure on the geometry of the structures is deeply investigated through optical emission spectroscopy (OES) and scanning electron microscopy (SEM). By analytically evaluating thermal beta (βt), directional beta (βd), and containment radii (Rs) for the plasma of the Cu–Zinc alloy, the validity of magnetic confinement has been proven. In general, five types of microstructures are produced: micro-sized spherical cones, mounted ablated networks, cavities, pores, ridges, and ablation channels with uplifted cones. Moreover, it has been found that, under a magnetic environment, the geometry of the structures is distinct and well-defined compared to those structures achieved when the ablation is carried out without applying a magnetic field.

Keywords: LIBS; Cu-alloy; ambient pressures; local thermal equilibrium; ns-LIBS; surface morphology

check for updates

Citation: Dawood, A.; Ahmed, N.; Bashir, S.; Hayat, A.; Sarfraz, S.M.A.; Ayub, A. Laser Ablation of Copper Alloy under Varying Environmental Conditions to Achieve Purpose-Built Surface Structures. *Coatings* **2022**, *12*, 1972. https://doi.org/10.3390/coatings12121972

Academic Editor: Jinyang Xu

Received: 15 November 2022
Accepted: 12 December 2022
Published: 15 December 2022

1. Introduction

Laser ablation offers a diverse range of uses, including thin-film manufacturing [1,2], micro fabrication [3,4], and medical applications [5,6], wherein the knowledge of the amount of mass eliminated as a function of experimental factors (including laser energy, atmospheric conditions, laser wavelength, and sample type) is essential for controlling and modelling the process. Laser-produced plasma is transitory in nature, with distinctive properties that change rapidly and are highly dependent on irradiation circumstances such as incoming laser intensity and pulse width, laser beam wavelength, irradiation spot size, and ambient gas composition and pressure [7–10]. The many processes involved in a laser ablation procedure, including laser absorption, evaporation, transient gas dynamics, radiation transport, condensation, ionization, and recombination, are rather complicated and require additional research [11]. For analyzing laser-produced plasma, numerous diagnostic methods are available, notably mass spectroscopy [12], Langmuir probe [13], microwave and laser interferometry [14,15], laser-induced fluorescence [16], Thomson scattering [17], photothermal beam deflection [18] and optical emission spectroscopy [8,19,20].

LIBS (laser-induced breakdown spectroscopy) is powerful an optical emission spectroscopy (OES) analytical technique capable of sampling solids, liquids, and gases for research and industrial applications [21–24]. A pulsed laser source is used to vaporize and excite a sample, resulting in the formation of a transitory plasma or plume that extends away from the sample surface. The optical emission resulting from the relaxation of excited species inside plasma provides information on the composition of the substance being examined. LIBS was initially a qualitative approach, but in recent years, it has evolved into a pseudo-quantitative micro-analysis tool for solids, liquids, and gases that can determine their elemental composition [25–27].

This study investigates plasma expansion in TMF to understand plasma dynamics [11], plume species spectrum intensity, plume refinement [28–30], and plasma instabilities [31]. EUV lithographic sources, debris reduction, thin film-deposition, nanoparticle synthesis, surface alterations, and LIBS detection-limits enhancement are key applications [32–34]. Externally applied TMF may influence plasma characteristics (optical spectrum intensity, T_e and n_e) and micro/nano surface structure.

Laser-produced plasma (LPP) has been proven to be confined in the presence of a TMF in many papers [28–30,35]. Patel et al. [36] studied brass plasma development in a non-uniform MF at low ambient pressures and atmospheric air pressures. MF divided the brass plume and intensified Cu (I) at 510.5 nm at low ambient gas pressures. Raju et al. [37] examined TMF's effect on Ba's LPP. Spectral intensity, Te, and ne were examined at various fluences (temporal variation). TMF improved LPP features. Rai et al. [38] examined how laser timespan affects LIBS performance in an external magnetic field and compact cavity. When laser-induced plasma is decelerated in a narrow cavity or by a continuous magnetic field, the LIBS signal increases. Magnetic fields doubled the LIBS signal. Theoretical research of decelerated plasma matched actual results, they said. Plasma confinement and laser duration affect LIBS signal growth. The plasma plume dynamics, electron–ion collision frequency, and LIBS signal saturation increase with laser intensity.

Corsi et al. [39] examined how crater depth influences plasma properties and LIBS emission. Despite plasmas being spatially and temporally resolved, they investigated plasma generation at the sample surface and at the bottom of the craters of the Cu sample. They measured plasma electron temperature and number density while studying LIBS emission. The craters' confinement effect increased laser-induced plasma LIBS signals. They also observed that crater walls limit plasmas. This confinement effect significantly affects laser-induced plasma characteristics and LIBS analysis outcomes. Rai et al. [40] examined how a transverse magnetic field (TMF) affected the LIBS of Mn, Mg, Cr, and Ti in aqueous solution. Line emission intensified 1.5-fold in TMF. They also found a significant rise in plasma emission between gate delays in TMF. After cooling the plasma, magnetic confinement increased plasma density and recombination rate, increasing emission. Magnetic confinement did not increase optical line emission in hot plasmas with strong background emission. Mg and Mn had half the LOD in the presence of a TMF.

Neogi et al. [31] examined carbon's LPP in vacuum and low ambient pressures with non-uniform TMF. They examined Te and ne under varied temporal and pressure conditions. TMFs raise all LPP properties temporally and at varying ambient pressures. Magnetic confinement, the $J \times B$ effect, Joule heating, and adiabatic compression raise LPP parameters. Abbasi et al. [17] used magnetic-field-aided LIBS and found an increase in optical emission from a palladium (Pd) sample. Plasma emission increased even at low laser fluence (12.6 J/cm^2). The magnetic field also enhanced the LPP parameters Te and ne.

Hussain et al. [41] investigated how an applied TMF affected LIBS emission with different air pressures and time delays of an Al sample. The 0.5 T magnetic field enhanced Al atomic lines at low pressure and shorter delay periods, whereas the Al (I) 396.1 nm spectral line signal rose 2-fold at 100 Pa and 100 ns. Electron impact excitation and recombination increased signal intensity with magnetic confinement. They examined plasma properties, including electron temperature and density. TMF increased compared to the field-free situation. Ping et al. [42] examined Al–Li LIBS at varying pressures and magnetic field intensity. A steady 1.1 T magnetic field increased Al I and Li I spectrum emission strength by 1.5–3 times. A fast ICCD camera captured time-resolved images of the laser-produced plume in their experiment. A magnetic field brightened plasma, persisted, and split the plume into two lobes. They also found that the magnetic confinement effect may increase excited atoms and high-energy species. Magnetically limited LIBS increased Te and ne.

Wang et al. [43] examined the use of a laser to generate artificial protrusions on metal surfaces. Stainless particles were melted using a diode-pumped solid-state laser system to create micron-sized protrusions on metal surfaces. They found that the strength and detachability of joints were significantly affected by the manufactured protrusions' shape and their adherence to the metal substrate. The joint's strength is diminished, however, if the huge protrusion damages the carbon fibers that are implanted in the polymer plate. They reported that, by manipulating the surface structures designed for that purpose, they might alter the surface morphology and produce a material surface suitable for the mechanical interlocking required to reinforce the metal/polymer junction.

Min et al. [44] reviewed the principle of laser ablation and its effect on the physicochemical properties of metallic materials. They described the application of purpose-built surface structures in order to modify their physicochemical properties and improve both the strength and durability of adhesive-bonded joints. They reported the mechanism accounting for the improved bonding strength and corrosion resistance of the adhesive-bonded joints fabricated from laser-ablated metallic materials. They discovered that the bonding strength of laser-ablated adhesively bonded joints increased as the roughness and wettability of the metallic adherend surface increased and that surface roughness contributed to improved joint strength only when the adhesive was capable of sufficiently wetting the laser-ablated surface to form mechanical interlocking at the bonding interfaces. Although laser-ablated surfaces were more active with lower polarization resistances and higher corrosion current, the increased roughness by laser ablation improved the corrosion resistance of laser-ablated adhesively bonded joints by retarding corrosive solution diffusion. As a result of their research, they reported that, among the several surface treatment options, laser ablation offers the most benefits in terms of efficiency, environmental friendliness, and ease of industrialization

Cu is a popular metal for plasma creation and laser ablation owing to its strong electrical conductivity and ductility. Copper plasma generated by a laser is also utilized to synthesize nanoparticles for usage in solar cells, sensors, LEDs, catalysts, antifungals, and anti-bacterial [45]. Cu–Zn alloy (Cu: 95% and Zn: 5%) is used for a variety of applications, including the coatings of slugs, the driving groups on certain artillery rounds, and the identification of enamelled and other jewels [45]. Typically, the sheet is used to manufacture metals by hammering. It is also utilized in silversmithing, notably as a low-cost preparation material [46]. Pure Cu metal has been extensively researched for LIBS, as well as for laser-induced structures, but little work has been provided on Cu-alloy, which is a very valuable industrial material [46].

The present work examines the impact of TMF on the plasma properties of laser-induced Cu-alloy at varying pressures of Ar, Ne, and He, and a link between surface structuring and plasma parameters is being created to improve their industrial uses. A 0.6 Tesla TMF is created using two permanent magnets. LIBS is utilized in the first series of experiments to explore the LPP of Cu in diverse ambient environments of Ar, Ne, and He at pressures ranging from 1 torr to 200 torr with a fixed optimum laser irradiance of 3.8 GW/cm^2.

2. Experimentation

2.1. Sample Preparation

We have chosen Cu–Zn alloy (Cu: 95% & Zn: 5%) purchased from Alpha Aesar for experimentation. Disk shaped samples were cut using CNC wire cutting. All targets were ultrasonically polished and cleaned before being mounted on a mechanical motorized translational stage under ultrahigh vacuum (UHV) conditions.

2.2. Measurements

Figure 1 shows a schematic depiction of the experimental setup. For material ablation and plasma formation, a Q-switch 1064 nm, 10 ns Nd: YAG laser (CFR200; Big Sky Laser Technologies, Quantel, France) is used. This laser has a 200 mJ pulse energy and a 10 Hz repletion rate.

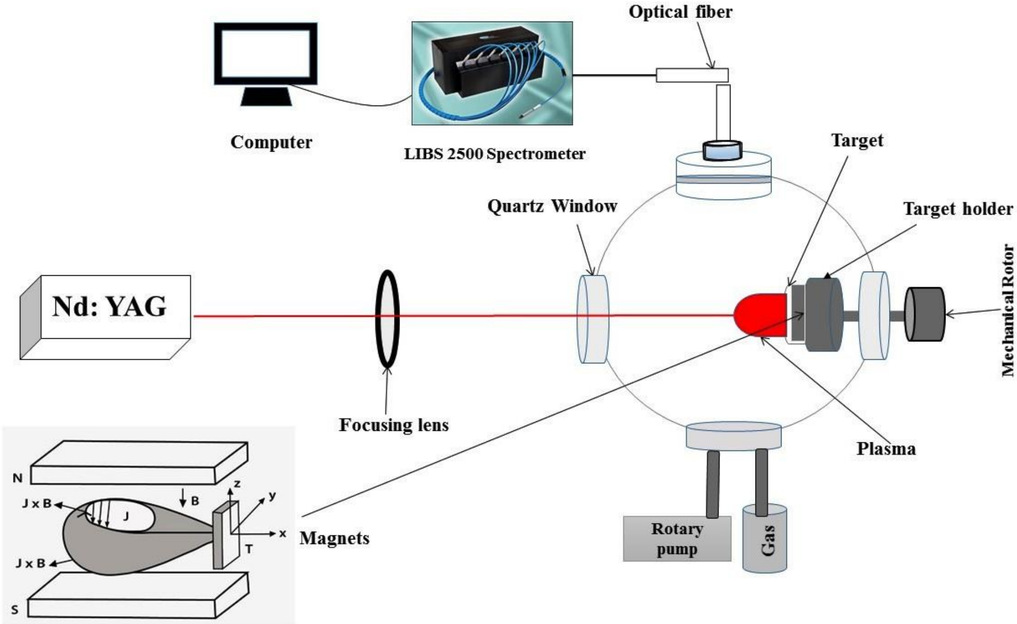

Figure 1. An experimental setup for studying the effect of TMF on the LIBS of Cu-alloy plasma generated with a Nd: YAG laser.

To create plasma, a lens with a focal length of 50 cm is used to focus the laser beam. Demtroder's formula is used to figure out that the size of the focused spot is 75 μm [47]. $\omega_f = \frac{\lambda f}{\pi\ \omega_o} = \frac{1064\ \text{nm} \times 50\ \text{cm}}{3.14 \times \frac{0.452}{2\ \text{cm}}} = 75$ μm where λ, f, ω_o represent the laser wavelength, focal length of the lens, and the beam radius without focusing, respectively. $M^2 = \frac{\theta}{\frac{\lambda}{\pi\omega_0}} = 1.5$ (approximately) is the beam quality factor. Therefore $\omega_f = 1.5 \times 75$ μm = 112.5 μm. The spot area by using the relation A= $\pi \times {\omega_f}^2$ is 3.97×10^{-4} cm^2. The spot area measured by SEM analysis is 3.94×10^{-3} cm^2. The target holder was progressively rotated with the assistance of a mechanical rotor to expose a fresh surface to each laser pulse. This is necessary to prevent the uneven pitting and cratering caused by each laser pulse. Targets were mounted in the vacuum chamber whose inner diameter was 24 cm, while the chamber's height was 18 cm. The chamber was evacuated at a rate of 300 L per second. After obtaining the needed vacuum, the system remained at that level for a minimum of one hour before being filled with the necessary gas. To examine the impact of the nature and pressure dependency of shield gases on the LIBS and surface morphology of laser-ablated Cu-alloy, the UHV chamber was filled with a variety of gases (Ar, Ne, and He). After the first refill, these ambient gases were flushed out of the chamber. Their pressure is precisely regulated with mbar accuracy.

The 0.6 Tesla TMF is created by using two disk-shaped (2 cm × 1 cm) permanent neodymium magnets. A Gauss meter (GM07 HIRST, Magnetic Instruments Ltd., Falmouth, UK) was used to quantify the magnetic field's intensity. TMF was implemented by positioning magnets 3 cm apart such that magnetic forces were perpendicular to the longitudinal plane of the LPP. The targets were then exposed to radiation in a variety of environmental conditions. Using a single cleaning shot, the LIBS surface was rendered contaminant-free. From a window set at 90 degrees to the direction of plasma expansion, we could see the bright plasma emission. In this case, a LIBS2500 plus spectrometer from Ocean Optics was used to capture the plasma's emission spectrum. For an investigation across a wide range of wavelengths, from 200 to 980 nm, this system uses a LIBS-fiber bundle equipped with seven linear silicon CCD array detectors, yielding an optical resolution of 0.1 nm.

Data from each spectrometer was collected in real time and saved on a computer using OOILIBS software (LIBS2500, Ocean Optics, Dunedin, Florida, USA, 200–980 nm, 2.1 ms) so that a comprehensive spectrum analysis could be generated. For this experiment, LIBS2500 triggered the Nd: YAG laser's Q-switch, while OOILBS controlled the laser's power output. All measurements had the same 1.25 μs delay between laser trigger and data collection. Plasma created by a single pulse decays or cools and produces light at various wavelengths for each element. A lens with a 5 cm focal length and a fiber-optic probe were used to capture the emission. After that, the signal was delivered to the spectrometer system.

Two sets of experiments were conducted.

1. Ar, Ne, and He were employed as background gases in the first set of experiments. Twenty pressures (1, 2, 3, 4, 5, 10, 20, 30, 40, 50, 60, 70, 80, 90, 100, 120, 140, 160, 180, and 200 torr) of inert gases were supplied for the experiment. These data were collected by exposing a Cu-alloy target to a single 150 mJ laser pulse at an intensity of 3.8 GW/cm^2 for 1.25 μs, then recording the resulting plasma emissions both without and with TMF.
2. A second series of studies were conducted to establish a relationship between the LPP parameters and the growth of surface structures. The Cu alloy target in this set was irradiated by 200 laser shots at 3.8 GW/cm^2 in a variety of environments, including Ar, Ne, and He at 1, 5, 30, and 50 torr pressure. The surface structures of laser-irradiated Mg alloy have been investigated using SEM examination. A scanning electron microscope (JEOL JSM 6490-A, Tokyo, Japan) was utilized for this analysis.

The LPP of Cu is defined by two plasma parameters, T_e and n_e. The T_e value is measured using the Boltzmann plot technique, whereas the n_e value is measured using the Stark broadening method. A second series of experiments was carried out for SEM analysis. An analytical computation of the plasma confinement characteristics, including thermal beta, directional beta, and containment radii, was performed in order to confirm that magnetic confinement works in the presence of 0.6 Tesla TMF.

3. Results

3.1. Effect of a Transverse Magnetic Field on LPP of Cu-Alloy

Figure 2 depicts the emission intensity of Cu (II) lines in the presence of the TMF (solid) and in the absence of the TMF (dashed) across the spectral range of 300 to 600 nm at an irradiation of 3.8 GW/cm^2 under Ar, Ne, and He at a pressure of 30 torr. In order to evaluate the LPP parameters, we chose four prominent Cu spectral lines at 324.52 nm, 327.21 nm, 447.99 nm, and 521.54 nm.

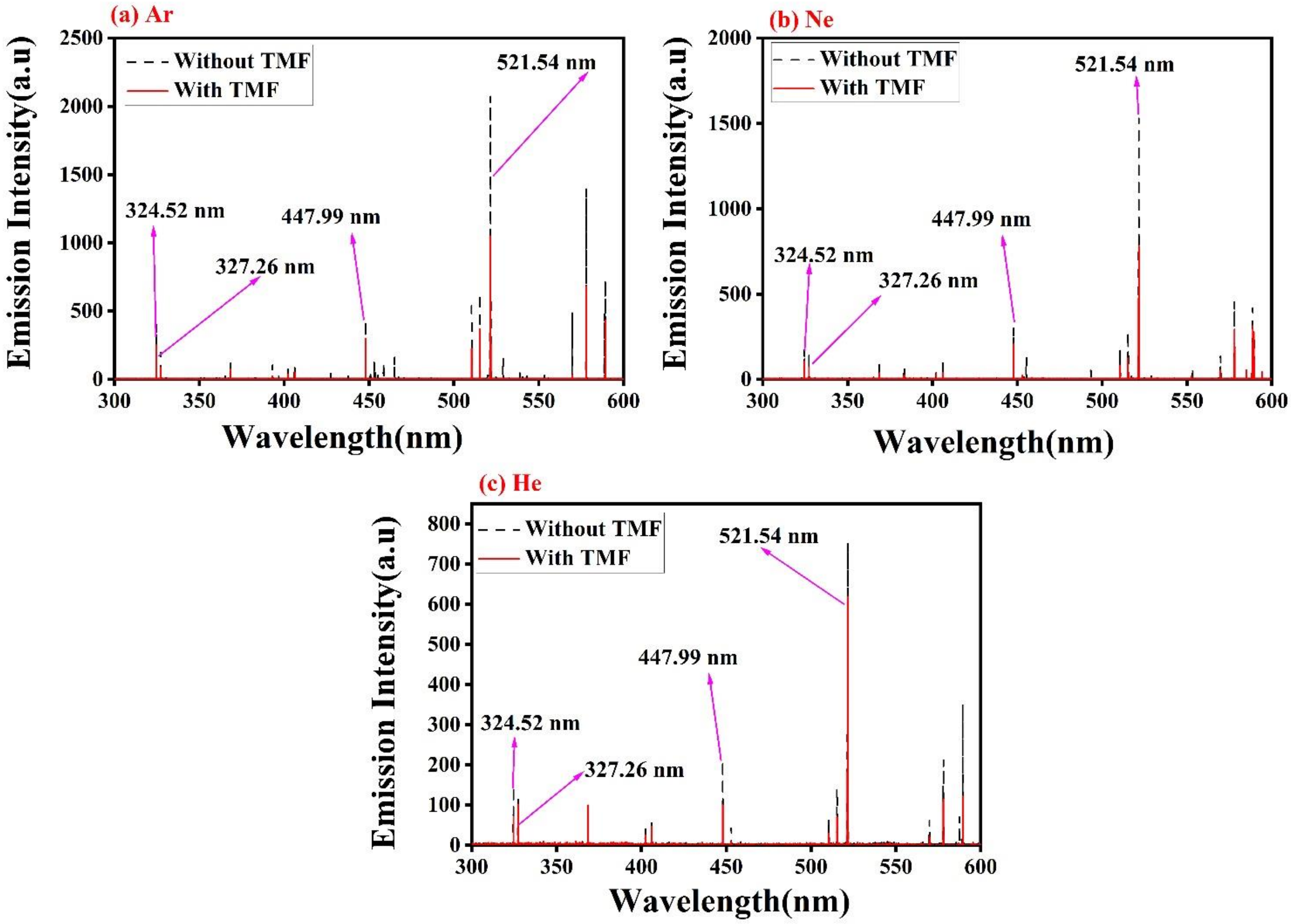

Figure 2. The optical emission spectra of selected Cu lines under 30 torr pressure of Ar, Ne, and He gas at 3.8 GW/cm^2 irradiance with and without TMF in the spectral range from 300 nm to 600 nm.

3.1.1. Investigation of Optical Emission Spectra of LPP of Cu-Alloy

Figure 3a,c,e show the variation in the spectral intensities of selected lines of Cu-alloy in the absence of TMF, whereas Figure 3b,d,f shows the variation in the spectral intensities of selected lines of Cu-alloy in the presence of TMF. All of the measurements were obtained at an intensity of 3.8 GW/cm^2 at a range of pressures in different environments with Ar (a and b), Ne (c and d), and He (e and f). In the field-free case, the spectral intensity increases until it peaks at 30 torr, drops to 100 torr, and finally saturates at higher pressures. Further, the presence of TMF significantly reduces the emission intensity compared to the field-free case. This is true in all cases. Ar has the highest emission intensity, followed by Ne, and then He. Furthermore, it is discovered that the presence of a TMF significantly reduces the emission spectrum intensity of Cu-alloy in comparison to the field-free scenario. All of the gases in the atmosphere behave this way. Several research groups have observed this, and they ascribe the slowdown to radiation recombination enhancement and/or deceleration [48–54].

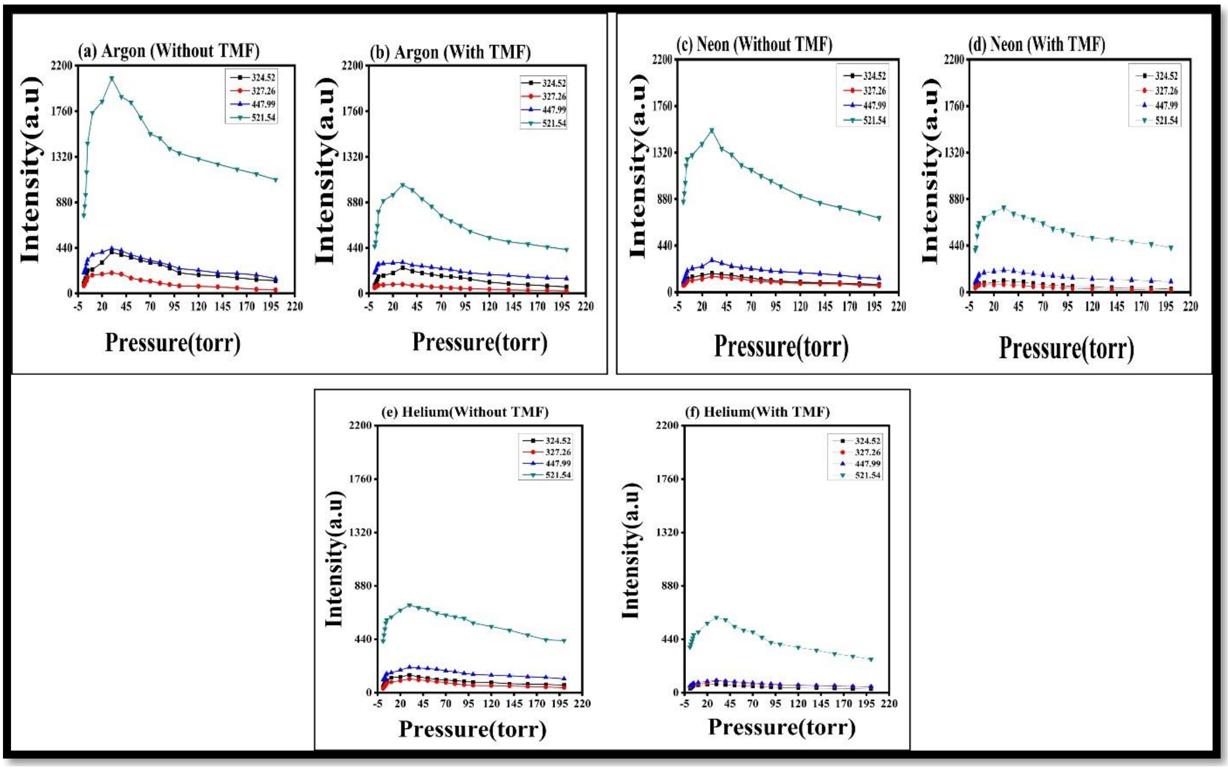

Figure 3. The spectral intensity variation of laser-induced Cu-alloy plasma under several pressure levels of the inert gases Ar (**a**,**b**), Ne (**c**,**d**), and He (**e**,**f**) at 3.8 GW/cm^2 irradiance.

The drop in spectral intensity is attributable to the decrease in the life time of higher states, which is a result of strong magnetic confinement effects [52]. Recombination lifetime is drastically reduced when TMF limits the plasma and prevents it from freely expanding. Consequently, there is a decrease in the spectrum intensity [53,55]. The decrease in radiative recombination and the rise in three-body radiative recombination [56] are both major contributors to the reduction in the Cu lines' spectral intensity. After the laser pulse terminates, the rapid fall in Te favors three-body recombination over radiative and/or dielectronic processes. With TMF present, the spectral intensity drops lower than in the field-free scenario because the life time for recombination falls dramatically as the plasma grows [51,55].

3.1.2. Investigation of Electron Temperature of Cu-Alloy Plasma

The Boltzmann plot technique has been used on spectroscopic data to calculate the Te of Cu plasma [52]. Assuming that the laser-induced plasma (LIP) is in a state of local thermodynamic equilibrium (LTE), using spectroscopic data, Te was calculated using a Boltzmann plot ($\ln\left(\frac{\lambda_{mn}\,I_{mn}}{g_m A_{mn}}\right) = -\left(\frac{E_m}{KT_e}\right) + \ln\left(\frac{N(T)}{U(T)}\right)$), with the parameters λ_{mn}, I_{mn}, g_m, A_{mn} describing the wavelength, intensity of the higher energy state, statistical weight, and transition probability, respectively. Higher-state energy (E_m), Boltzmann constant (k), electron temperature (T_e), total number density (N (T), and partition function (U (T)) are shown on the right. Figure 4 displays the Boltzmann plot of selected Cu-plasma lines. Table 1 displays the spectroscopic parameters required for Te analysis, which are retrieved from the NIST database [57] and the atomic line list [58]. Figure 5a without TMF and 5b with TMF show the change in Te for different ambient gases when the pressure is varied from 1 to 200 torr while the irradiance is held constant at 3.8 GW/cm^2.

Table 1. Spectroscopic parameters of Cu II lines obtained by NIST database and literature [57,58].

Spectroscopic Data				
Wavelength (nm)	Transitions	Energy of Upper Level E_m (cm^{-1})	Statistical Weight g_m	Transition Probabilities ($10^8 S^{-1}$)
324.52	$3d_9.5p–3d_9.7d$	153,821.94	5	5.95×10^{-3}
327.26	$3d_8.(3F).4s.4p.(3P_o)–3d_9.(2D<3/2>).7s$	146,936.32	5	2.00×10^{-4}
447.99	$3d_9.4d–3d_9.6p$	138,401.95	7	2.16×10^{-4}
521.54	$3d_{10}.9p \rightarrow 3_9.4s.(3D).7s$	134,742.85	9	5.41×10^{-4}

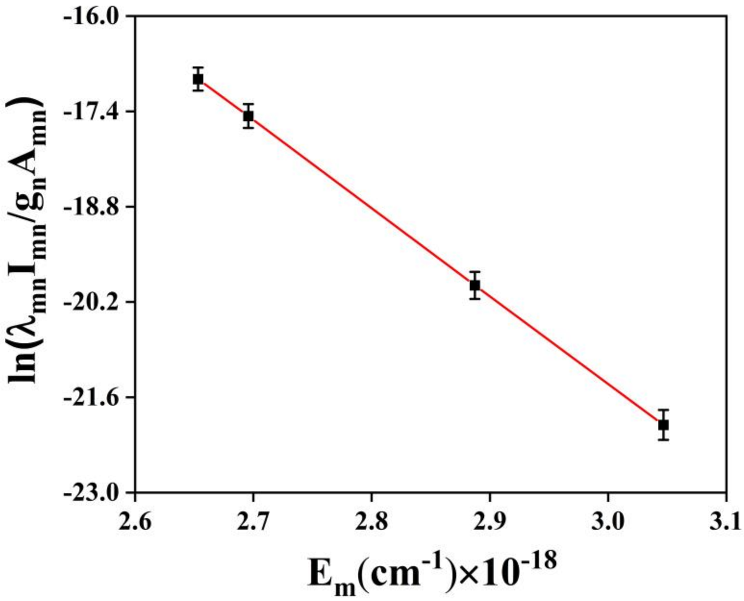

Figure 4. The slope of Boltzmann plot obtained by using spectroscopic data of laser-ablated Cu.

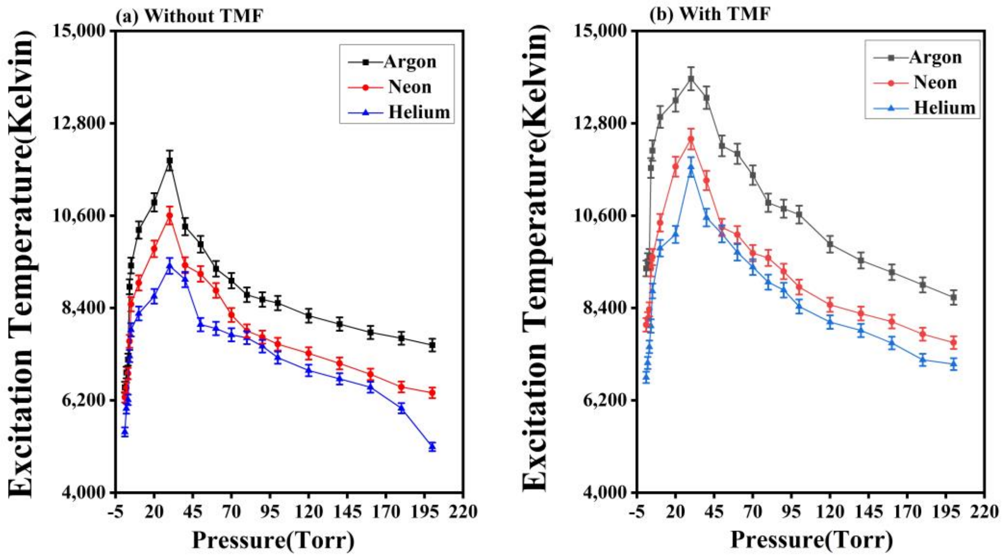

Figure 5. The change in Te of laser-induced Cu-alloy plasma at different pressures in Ar, Ne, and He environments at 3.8 GW/cm^2 ns laser irradiance in the absence (**a**) and presence (**b**) of TMF.

The Te of the LPP of Cu-alloy ranges from 6513 K to 11,915 K for Ar, 6278 K to 10,605 K for Ne, and 5449 K to 9404 K for He in the absence of TMF. Ar has Te values between 8653 K and 13,864 K, Ne between 7577 K and 12,427 K, and He between 6750 K and 11,760 K when a TMF is applied. Te increases monotonically up to a maximum at 30 torr, regardless of the presence or absence of TMF. After that, we see a drop in Texc from 40 to 200 torr. In both the absence and presence of TMF, the Te value of Cu plasma is greatest when associated with Ar, compared to Ne and He.

3.1.3. Investigation of Electron Number Density of Cu-Alloy Plasma

Cu LPP's time-integrated ne is evaluated using the Stark-broadening ($\Delta\lambda_{\frac{1}{2}} = 2\omega\left(\frac{N_e}{10^{16}}\right) + 3.5A\left(\frac{N_e}{10^{16}}\right)^{\frac{1}{4}}\left[1 - 1.2N_D^{\frac{-1}{3}}\right] \times \omega\left(\frac{N_e}{10^{16}}\right)$) technique [59]. Lorentzian fitting is used on the Cu (II) spectral line at 327.26 nm to determine the ne of Cu-alloy plasma (Figure 6).

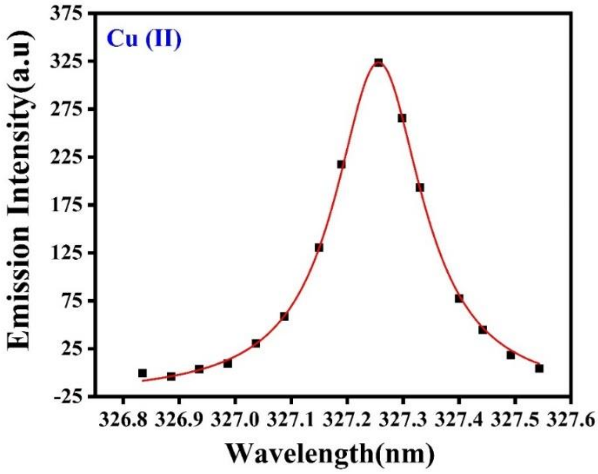

Figure 6. A Lorentzian fit of 327.26 nm line used for calculation of electron number density of Cu-plasma.

In Figure 7a,b, we depicted the ne of laser-produced Cu-alloy plasma variation in the absence (left) and presence (right) of TMF at 3.8 GW/cm^2 irradiation and in the Ar, Ne, and He environments, respectively.

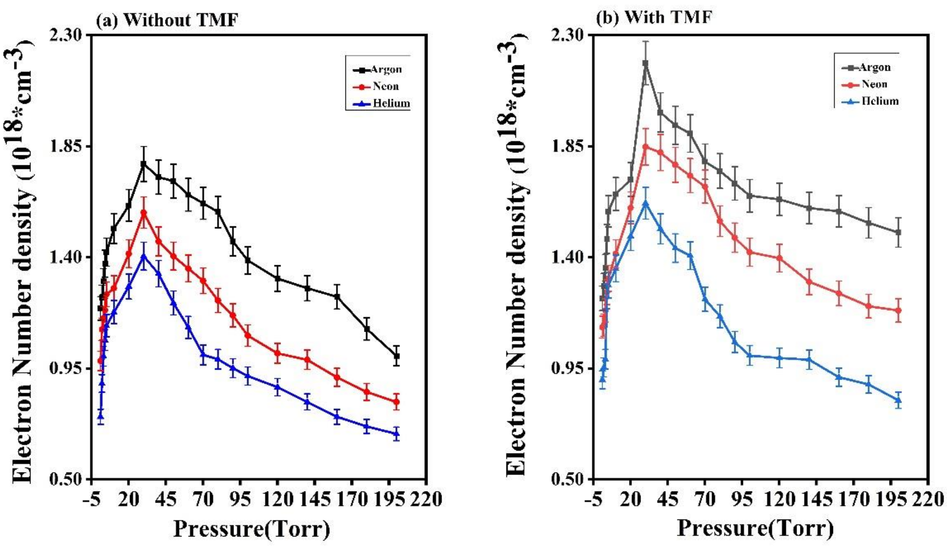

Figure 7. The variation in n_e of laser-induced Cu-alloy plasma at various pressures under Ar, Ne, and He environments at an irradiance of 3.8 GW/cm^2 in the absence (**a**) and presence (**b**) of TMF.

Cu plasma's ne fluctuates from 1.0 $\times$ 10^{18} cm^{-3} to 1.78 $\times$ 10^{18} cm^{-3} for Ar, 0.81 $\times$ 10^{18} cm^{-3} to 1.58 $\times$ 10^{18} cm^{-3} for Ne, and 0.69 $\times$ 10^{18} cm^{-3} to 1.41 $\times$ 10^{18} cm^{-3} for

He in a field-free scenario. For TMF, the values of ne for Ar are between 1.23×10^{18} cm^{-3} to 2.19×10^{18} cm^{-3}; for Ne, they range from 1.12×10^{18} cm^{-3} to 1.85×10^{18} cm^{-3}, and for He, they vary from 0.82×10^{18} cm^{-3} to 1.62×10^{18} cm^{-3}. After a linear increase from 1 to 20 torr, the ne of Cu plasma plateaus at 30 torr. As pressure is increased from 40 torr to 200 torr, ne is found to be decreasing. Every single environmental gas follows this pattern (Ar, Ne, and He). However, Ar has a higher ne of Cu in laser-induced plasma than Ne and He. Similarly, ne is enhanced in TMF under all environmental conditions.

4. Discussion

It has been reported by a large number of research groups [60] that the characteristics of LPP are strongly reliant on the type and pressure of the surrounding gases. The findings obtained from the LIBS demonstrate that the emission intensity, electron temperature, and density are highly impacted not only by the ambient environment but also by the pressure change of that atmosphere.

Emission intensity, electron temperature, and electron density are all found to be greatest for Ar, next for Ne, and finally for He, where they are at their lowest. When pressure is increased, the temperature and density of the gas's electrons both rise to a maximum, whereupon they then begin to fall monotonically with subsequent increases in pressure. Both the temperature and the electron density are found to be at their highest at 30 torr, regardless of the surrounding pressure. At pressures up to 30 torr for Ar, Ne, and He, an increasing trend in Te and ne of Cu plasma was seen (Figures 5 and 7), which was ascribed to a diminished shielding effect of the ambient gas plasma as a result of a decreased gas particle density at lower pressures. In a low-pressure environment, plasma spreads easily into that area, reducing the density of species inside the plasma.

As a consequence, the target surface is less shielded from the laser pulse and experiences less absorption through inverse bremsstrahlung. When the pressure is high enough, the collision frequencies of plasma particles increase, leading to a greater amount of momentum transfer [61] and a more rapid expansion of electron cascades. The surrounding gas plasma also serves as a kind of energy buffer, imparting some of its own heat to the plasma of the surrounding substance. Therefore, more energy is focused on the surface, yielding a bigger quantity of ablated material and thus raising the electron density and temperature [62,63].

Maximum electron density and temperature are seen when pressure is raised up to 30 torr in all ambient circumstances; this is due to the confinement effect of plasmas [64]. In conclusion, our findings suggest that the spectrochemical features of laser-induced plasmas may be enhanced by using Ar, Ne, or He as the ambient gas at certain filled pressures. When the pressure is raised from 40 to 200 torr, the plasma is confined even closer to the surface of the target, which shields the target surface. A large portion of the pulse is absorbed by the plasma, leading to significant shielding that lowers the amount of mass ablated from the target [65]. The plasma (the first ablated material) absorbs more of the laser pulse energy, yet at that pressure, the measured plasma temperature and electron density are lower. This may be explained as follows: as the ambient pressure is raised, the number of times an electron collides with an atom in the background gas rises elastically. Since the rate of increase in the energy of free electrons through inverse bremsstrahlung is larger than the rate at which the cascade condition is preferred, the temperature is lower at greater pressure [64,66].

The reason that Ar has greater Te and ne values than Ne and He is because of cascade development and elastic collisions, as given by $Q_{\Delta t} = \frac{2m_e}{M_B} \sigma_{ea} n_B \left(\frac{5KT_e}{\pi m_e}\right)^{\frac{1}{2}}$ [62], where n_B is the density of atoms in the background gas, M_B is the mass of the background gas, and σ_{ea} is the elastic scattering cross section of electron atoms. The relation states that the rate of cooling of LPP is proportional to the inverse of the mass of M_B. Inferred from this is the fact that gases with a lower density cool more rapidly than those with a higher density. As M_B grows, the efficiency with which particles transmit their energy to one another via collision decreases, extending the lifetime of LPP. The LPP cools down more quickly, reducing the plasma's lifetime, if the thermal conductivity is high [67]. The presence of TMF reduces the emission intensity of all ambient gases compared to when TMF is absent.

In light of Rumbsy and Paul's relation, we may understand why there is a decrease in emission strength when TMF is present. Their relation $\frac{3\times10^{19}\mathrm{T_e}^{3.75}}{Z}$ m^{-3} shows that three-body recombination would predominate over radiative recombination if the predicted ne is larger than $\frac{3\times10^{19}\mathrm{T_e}^{3.75}}{Z}$ m^{-3}.

The analytical assessment of Cu-plasma puts its ne in the region of 10^{19} m^{-3}, whereas our experimental determination places it in the 10^{24} m^{-3} range. These results provide more evidence for the veracity of three-body recombination and provide credence to the claim that spectral intensity decreases once TMF is utilized. Te and ne values for Cu-alloy in TMF are higher than in the field-free scenario in all ambient gases. In TMF, the expansion of plasma is accompanied by a separation of plasma species due to the Lorentz force operating perpendicular to the direction of plume growth. This implies that LPP may spread in both axial and radial directions. The LPP plasma front slows down in both directions, even though its radial velocity is lower than its axial velocity.

We assessed certain analytical indicators, including thermal beta, directed beta, and confinement radius, to verify the reliability of the implemented TMF. The thermal β_t is a critical factor when expanding into a magnetic field. β_t of the plasma is given as $\beta_t = \frac{8\pi n_e K T_e}{B^2}$ [52], where B is the magnetic field (G), ne is the density in cm^{-3}, k is the Boltzmann constant, and *Te* is the temperature in eV. When the LPP pressure is equal to the plasma pressure, the plume will cease expanding (β_t = 1). If $\beta_t > 1$, magnetic confinement does not occur, whereas if $\beta_t < 1$, magnetic confinement does occur. As the plasma's kinetic pressure increases relative to the magnetic fields, the LPP will eventually break through the field's core. The plume's internal pressure drops because the magnetic field penetrates deeper into the plasma and slows its expansion. If the field exerts a pressure equal to that of the kinetic pressure, then the LPP will be compressed and confined.

In Tables 2–4, we can see how β_t shifts in response to varying pressures for Ar, Ne, and He. Figure 8 is a diagrammatic representation of the aforementioned values, showing how β_t varies with pressure. At a pressure of 30 torr, when the Te and ne of Cu-plasma are both at their highest, the maximum value of β_t is attained.

Expanding plasma has a β_d of the order of a few hundred at the outset, indicating that the LIP of Cu-alloy is in the diamagnetic domain [69]. The diamagnetic cavity of the LPP becomes larger, and the magnetic energy is equalized with the total energy of the plasma. This LPP will be slowed by the combined impact of magnetic pressure and the pressure applied by the surrounding gas. If we assume that the plasma grows spherically, we may calculate the radius within which the magnetic field is confining the plasma. Using the relation [45], $R_b = \left(\frac{3F_{la}A_l}{2\pi\left(\frac{B^2}{2\mu_o}+P_{air}\right)}\right)^{\frac{1}{3}}$ where F_{la} is the absorbed laser fluence, we may calculate the confinement radius. When we use a wavelength of 1064 nm and a laser fluence of 44.4 $\mathrm{J/cm^2}$, the resulting F_{la} is 1.3 $\mathrm{J/cm^2}$, and the corresponding value for the confinement radius is 13 mm. It uses the fact that plasma will be greatly slowed down up to a distance of 13 mm at a pressure of 30 torr and a laser irradiation of 3.8 $\mathrm{GW/cm^2}$.

It is important to note that the nature of the surrounding gases may have a significant impact on plasma values. Since Iida et al. [66] established the necessary conditions for cascade growth, this trend may also be understood in that context. According to their study, the E/M (charge/mass) ratio is the sole factor that matters for calculating the energy dissipated during cascade growth. The values for Ar, Ne, and He are 0.53, 1.08, and 6.04, respectively. This proves that Ar is preferable than Ne and He in terms of cascade growth. Therefore, it is clear why the emission intensity, Te, and ne of Cu-alloy plasma in Ar is greater than that of Ne and He plasma.

Table 2. Evaluated T_e, n_e, β_t, and β_d values for laser-irradiated Cu-alloy plasma at various Ar pressures in the presence and absence of TMF.

Argon						
Pressure	**T_e (Kelvin)**		**n_e (10^{18}) (cm^{-3})**		**Analytical Parameters**	
	Without TMF	**With TMF**	**Without TMF**	**With TMF**	**Thermal Beta**	**Directed Beta**
1	6513	9344	1.19	1.23	0.30	79
2	6864	9515	1.24	1.28	0.32	83
3	7171	9616	1.30	1.36	0.36	93
4	8907	11,737	1.38	1.48	0.43	107
5	9413	12,152	1.42	1.59	0.51	112
10	10,259	12,954	1.52	1.66	0.68	136
20	10,919	13,346	1.61	1.72	0.70	150
30	11,915	13,864	1.78	2.19	0.76	163
40	10,341	13,411	1.72	1.99	0.62	154
50	9922	12,264	1.71	1.94	0.58	135
60	9336	12,075	1.65	1.90	0.56	121
70	9053	11,567	1.62	1.79	0.51	102
80	8715	10,909	1.58	1.75	0.46	95
90	8603	10,767	1.46	1.70	0.40	85
100	8519	10,627	1.39	1.65	0.38	76
120	8218	9922	1.3	1.64	0.35	70
140	8019	9536	1.28	1.60	0.34	65
160	7819	9253	1.24	1.59	0.32	60
180	7681	8953	1.11	1.54	0.31	54
200	7519	8653	1.00	1.50	0.30	50

Table 3. Evaluated T_e, n_e, β_t, and β_d values for laser-irradiated Cu-alloy plasma at various Ne pressures in the presence and absence of TMF.

Neon						
Pressure	**T_e (Kelvin)**		**n_e (10^{18}) (cm^{-3})**		**Analytical Parameters**	
	Without TMF	**With TMF**	**Without TMF**	**With TMF**	**Thermal Beta**	**Directed Beta**
1	6278	8000	0.98	1.12	0.25	64
2	6496	8139	1.11	1.13	0.27	67
3	6841	8368	1.15	1.19	0.31	75
4	7609	9340	1.19	1.26	0.34	89
5	8491	9616	1.25	1.32	0.45	100
10	9000	10,432	1.28	1.42	0.50	118
20	9810	11,768	1.42	1.60	0.52	129
30	10,605	12,427	1.58	1.85	0.63	148
40	9421	11,440	1.47	1.83	0.60	131
50	9214	10,322	1.41	1.78	0.52	115
60	8820	10,149	1.36	1.73	0.51	102
70	8236	9709	1.31	1.69	0.45	94
80	7855	9595	1.23	1.55	0.41	85
90	7708	9272	1.17	1.48	0.38	74
100	7541	8900	1.08	1.42	0.35	64
120	7320	8477	1.01	1.40	0.31	53
140	7080	8270	0.99	1.30	0.29	50
160	6820	8077	0.91	1.25	0.27	45
180	6520	7777	0.86	1.20	0.25	42
200	6380	7577	0.81	1.19	0.22	40

Table 4. Evaluated T_e, n_e, β_t, and β_d values for laser-irradiated Cu-alloy plasma at various He pressures in the presence and absence of TMF.

Helium						
Pressure	**T_e (Kelvin)**		**n_e (10^{18}) (cm^{-3})**		**Analytical Parameters**	
	Without TMF	**With TMF**	**Without TMF**	**With TMF**	**Thermal Beta**	**Directed Beta**
1	5449	6750	0.75	0.90	0.22	53
2	6006	7093	0.89	0.95	0.23	59
3	6213	7476	0.99	1.01	0.24	63
4	7257	7974	1.07	1.24	0.28	75
5	7881	8806	1.12	1.29	0.36	91
10	8271	9827	1.18	1.36	0.42	93
20	8681	10,154	1.28	1.49	0.47	105
30	9404	11,760	1.41	1.62	0.58	129
40	9080	10,555	1.33	1.52	0.45	107
50	8006	10,170	1.22	1.44	0.40	99
60	7913	9727	1.12	1.41	0.37	91
70	7762	9378	1.01	1.23	0.35	78
80	7693	9017	0.99	1.16	0.33	70
90	7490	8827	0.95	1.06	0.32	64
100	7218	8438	0.92	1.00	0.31	58
120	6913	8066	0.87	0.99	0.29	41
140	6713	7866	0.81	0.98	0.26	39
160	6513	7566	0.75	0.91	0.25	35
180	6013	7166	0.71	0.89	0.22	31
200	5093	7066	0.69	0.82	0.20	28

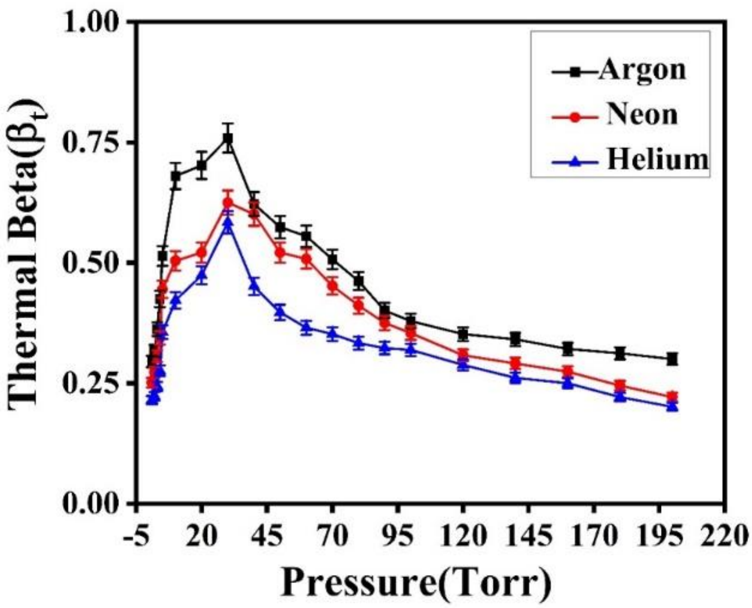

Figure 8. The variation in thermal beta of laser-induced Cu alloy plasma at various pressures under Ar, Ne, and He environments at ns laser irradiance of 3.8 GW/cm^2.

According to the published research [51], using a magnetic field to slow down a plume's progression does not prevent it from progressing at all. Thus, β_t is not the sole relevant parameter; directional β_d is also crucial in describing plasma confinement [68]. Once thermal energy has been transformed into directed energy, β_d may be calculated using the relation $\beta_d = \frac{4\pi n_e(3K_B T_e)}{B^2}$ [68]. We calculate the directed β_d for a range of ne and T_e in Cu-alloy plasma at different pressures of different ambient circumstances. Magnetic confinement is validated by the fact that magnetic pressure is always greater than plasma pressure. Tables 2–4 show the resulting changes in β_d of Cu plasma when pressure is varied in Ar, Ne, and He ambient conditions, respectively. Figure 9 provides a visual representation of these values, showing how βd varies with the pressure of the surrounding gases.

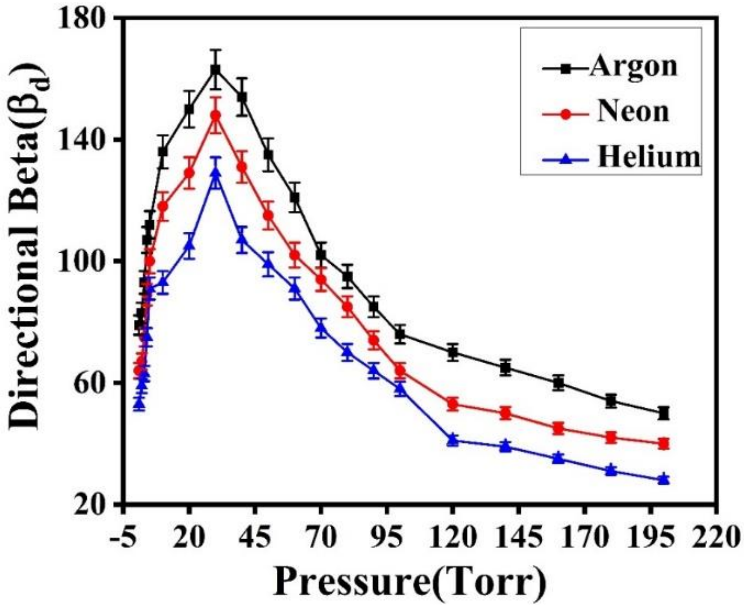

Figure 9. The fluctuation in directional beta of laser-induced Cu alloy plasma at different pressures in Ar, Ne, and He environments at 3.8 GW/cm^2 ns laser irradiation.

4.1. Investigation of Surface Analysis of Laser-Irradiated Cu Alloy

SEM analysis is used to investigate how exposure to a magnetic field affects the surface changes of laser-irradiated Cu-alloy. As such, the Cu targets were subjected to 200 laser pulses at a fixed laser energy of 150 mJ, equivalent to a laser irradiance of 3.8 GW/cm^2, in three distinct environments of Ar, Ne, and He at varied pressures (1 torr, 5 torr, 30 torr, and 50 torr).

4.1.1. Surface Morphology of Cu-Alloy under Ar Environment without TMF

SEM images of Figure 10a–d exhibit the surface morphology of the laser ablated area of Cu-metal without a magnetic field under Ar environment at different pressures of 1, 5, 30, and 50 torr.

The diffusive cones, cavities, droplets, and non-uniform melting are prominent features of all pressures. For the lowest pressure of 1 torr, the non-uniform spherical-top-headed cones and cavities are observed in Figure 10a. The number of cones and their size decrease at 5 torr in Figure 10b. By increasing the pressure, the cones and cavities vanished. The molten material and droplets are seen and decrease by increasing the pressure. Turbulent melt flow is also seen between the periodic ridges. The excessive laser energy interaction to the target surface material detaches the material in the form of droplets [70]. The temperature gradients and pressure gradients are produced due to the laser-induced heating and vaporization on the target surface, which is responsible for the expansion of molten material that can account for droplets formation [52].

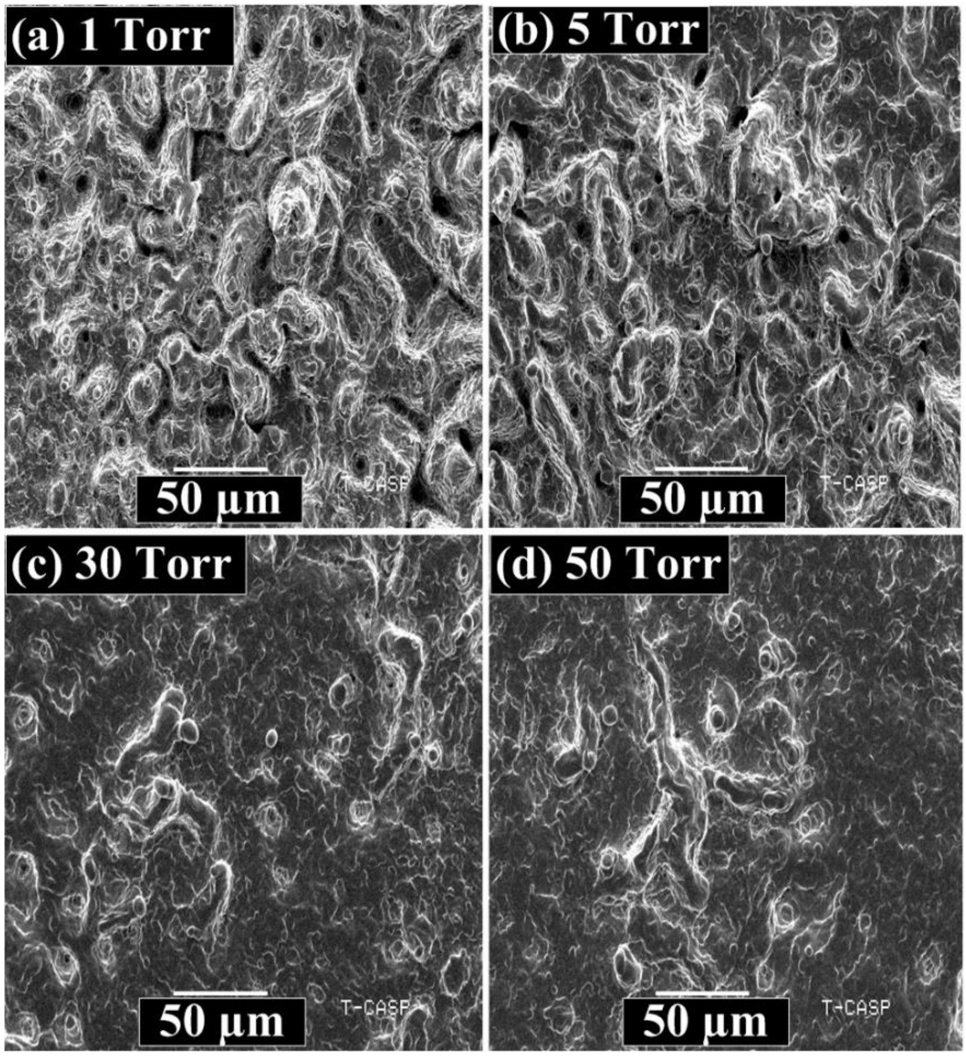

Figure 10. SEM micrographs illustrating surface morphological variations in an Ar ambient environment at various pressures, respectively (**a**) 1 torr, (**b**) 5 torr, (**c**) 30 torr, and (**d**) 50 torr, with a laser irradiation of 3.8 GW/cm^2 in the field-free condition.

4.1.2. Surface Morphology of Cu-Alloy under Ar Environment with TMF

SEM micrographs of Figure 11a–d exhibits the modified laser-ablated area of Cu-metal with a magnetic field under Ar environment after irradiation at different pressure of 1, 5, 30, and 50 torr.

The distinct uplifted micro-sized cones, cavities, ridges, and non-uniform melting are prominent features for all pressures. For the lowest pressure of 1 torr, the large-scale melting, micro-sized spherical cones, and cavities are seen in Figure 11a. The micro-sized conical structures are formed in three steps. In the first step, the precursor sites are formed, i.e., roughness present on the target surface and surface defects before the laser matter interaction and laser induced micro/nano structures. In the second step, the laser light scattering from these precursor sites results in the increased laser energy and excessive ablation in the valleys between these precursor sites and finally the evolution of these sites into micro-sized conical structures on the target surface. In the third step, the growth and merging of cones occur [71,72].

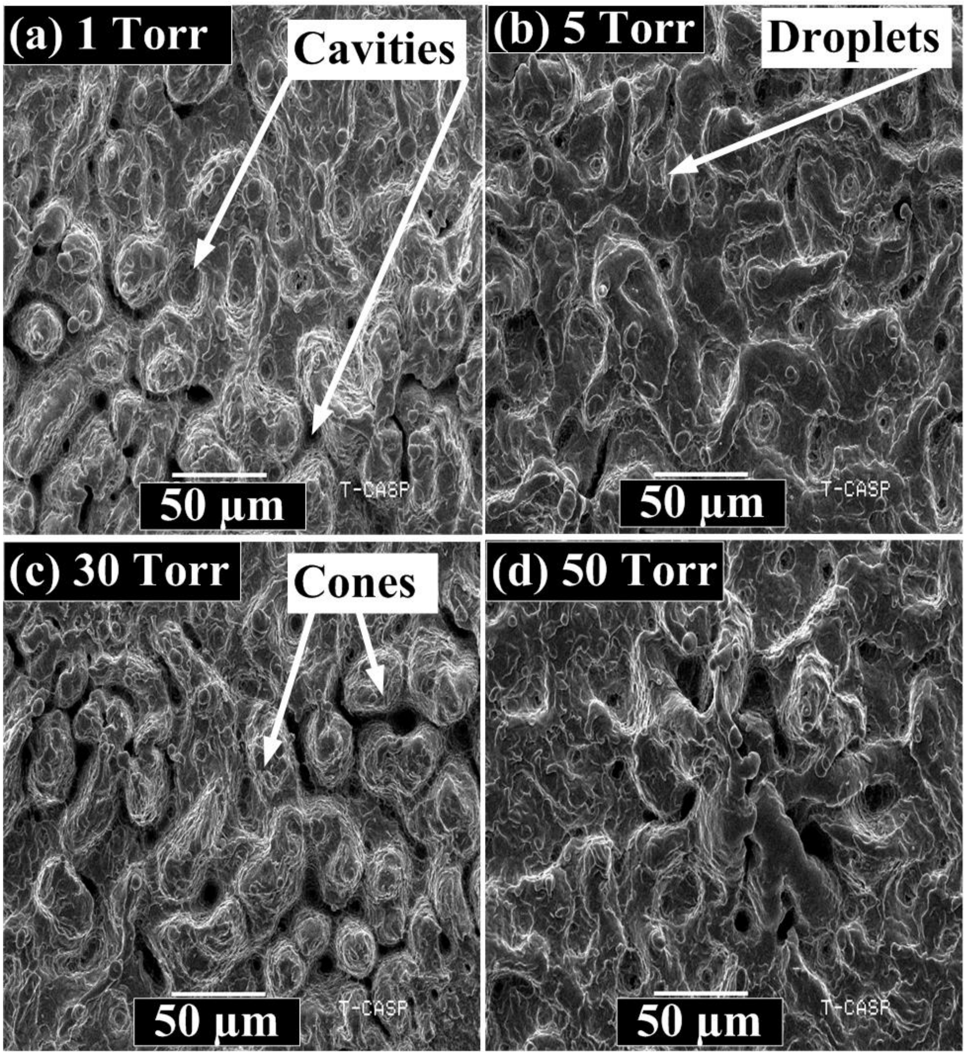

Figure 11. Surface morphological modifications in an Ar ambient environment at different pressures, (**a**) 1 torr, (**b**) 5 torr, (**c**) 30 torr, and (**d**) 50 torr, with a laser irradiation of 3.8 GW/cm^2 in the TMF.

Another possible reason for the growth of micro-sized spherical cones is that stresses and depressions are generated on the target surface due to incoming laser light. Relaxation of these stresses and depressions finally evolves into cones when laser pulse is finished, also accounted for cone formation [52,73,74].

In the underlying pores, the gases are absorbed due to the rapid volume expansion and heating of the subsurface layer which is responsible for cavity formation [75]. Under the superficial layer, the relaxation of mechanical stresses may be another possible reason for cavity formation [76–78]. The different sizes of cavities are due to the contaminations, inclusions, and small pits on the target surface [79–81]. Increasing the pressure from 1 torr to 5 torr, the non-uniform melting diffusive cones are ridges formed and visible in Figure 11b. Ridges are formed due to the abrupt expulsion of molten material towards the boundary by the recoil pressure of plasma [82].

In Figure 11c, the uplifted micro-sized cones and cavities are seen. The number of cones increase by increasing the pressure. The non-uniform molten material is seen, and cones are vanished in Figure 11d at a final pressure of 50 torr.

4.1.3. Surface Morphology of Cu-Alloy under Ne Environment without TMF

SEM micrographs of Figure 12a–d show the laser-ablated area of Cu-metal without a magnetic field under a Ne ambient gas environment at different pressures of 1, 5, 30, and 50 torr. For all pressures, the irregular cones and splashed molten material are prominent features. In Figure 12a, at the lowest pressure of 1 torr, the regular diffusive spherical cones are seen at the center. At the outer edges, tiny droplets are observed. In Figure 12b, the size of cones and density of cones is increased, along with the formation of cavities and droplets. The size and density of cones is decreased in Figure 12c. The droplets are more prominent. As the pressure increased from 30 torr to 50 torr the flower structure is seen. The cones in the flower structure are diffusive and irregular. At the outer edges, the large-size cones are visible.

4.1.4. Surface Morphology of Cu-Alloy under Ne Environment with TMF

SEM micrographs of Figure 13a–d represent the modified laser-irradiated area of Cu-metal with a magnetic field under Ne environment at different pressures of 1, 5, 30, and 50 torr. For all pressures, the spherical cones, cavities, and droplets are dominant structures. In Figure 13a, for the lowest pressure, uniform spherical-top-head cones are observed. The droplets at the top head of the spherical cones are seen.

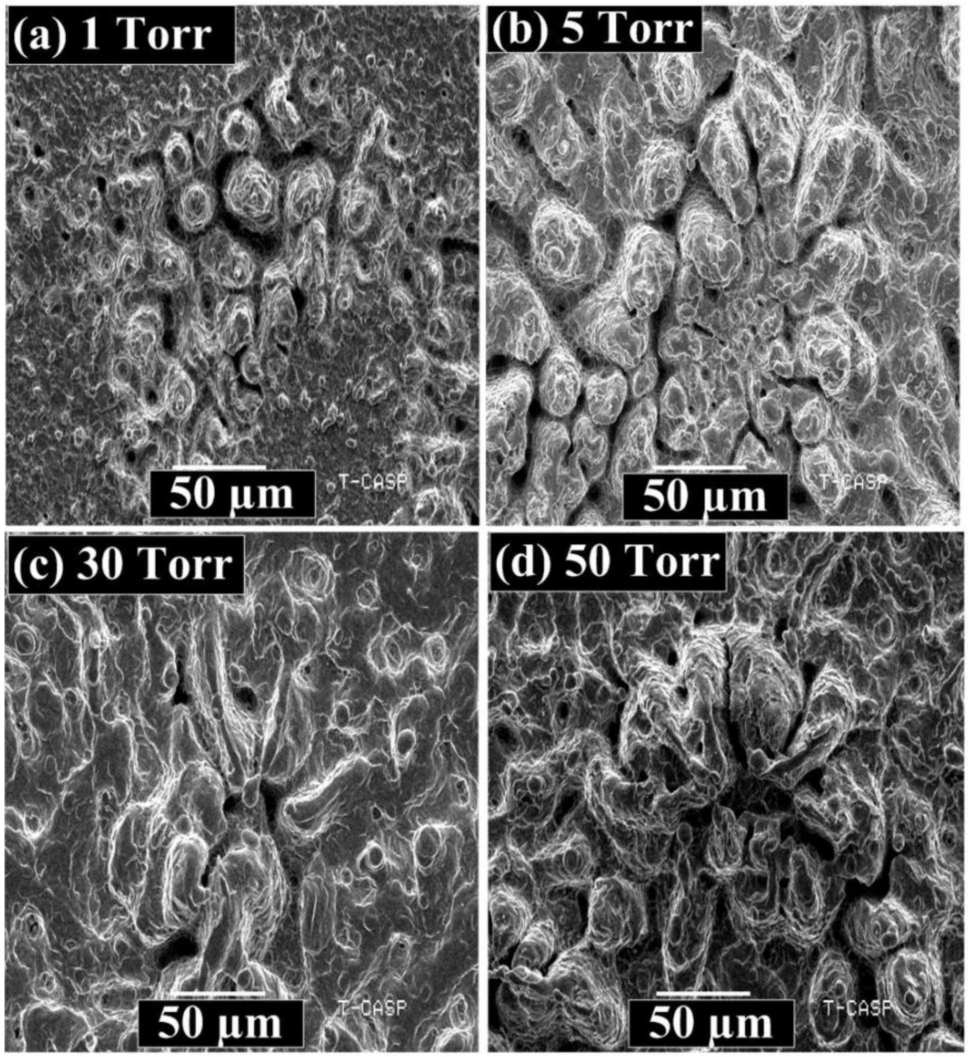

Figure 12. SEM micrographs exhibiting the variation in surface morphology under an ambient environment of Ne at different pressures, viz., (**a**) 1 torr, (**b**) 5 torr, (**c**) 30 torr, and (**d**) 50 torr, with a laser irradiance of 3.8 GW/cm^2 in the field-free case.

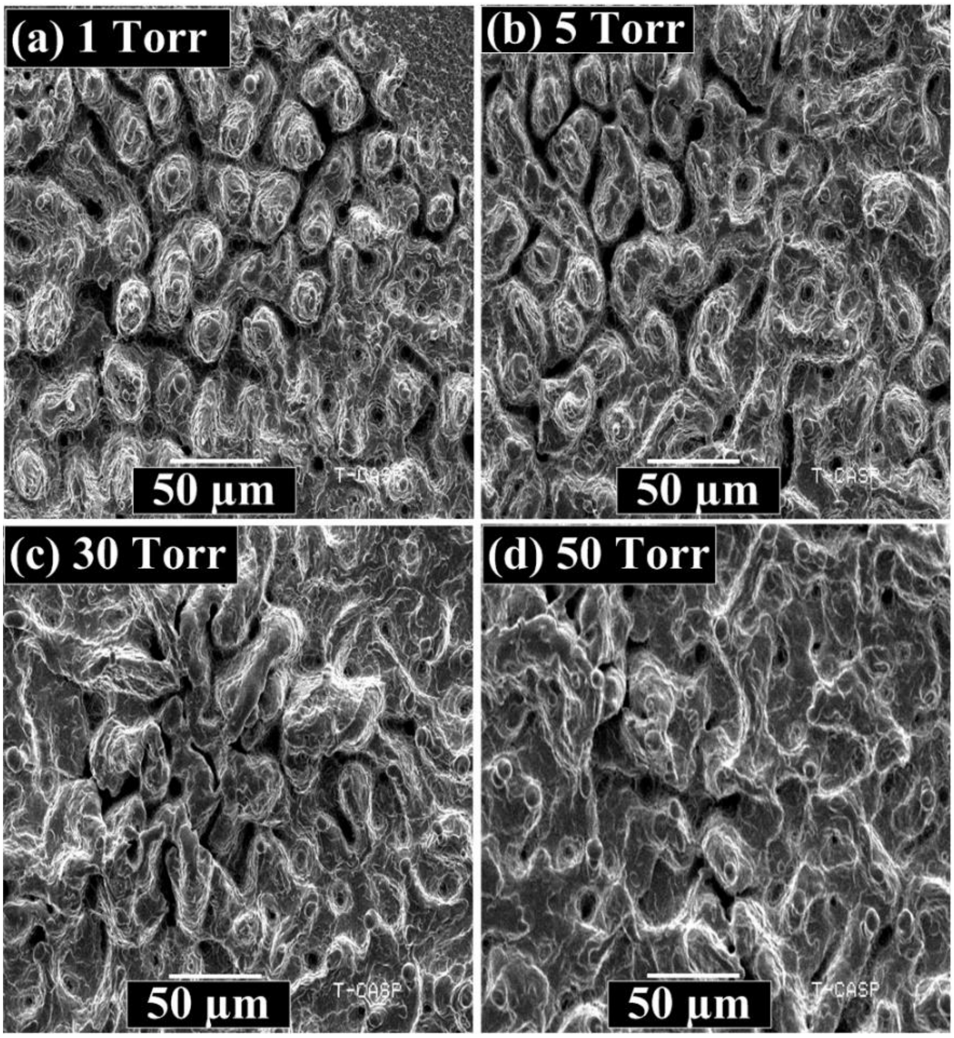

Figure 13. Surface morphological modifications in a Ne ambient environment at different pressures, (**a**) 1 torr, (**b**) 5 torr, (**c**) 30 torr, and (**d**) 50 torr, with a laser irradiation of 3.8 GW/cm^2 in the TMF.

The non-uniform cavities between the cones are observed. For a pressure of 5 torr, the uniformity of spherical-top-head cones is decreased. The laser-induced molten material and groove-like cavities are seen. In Figure 13c, the irregular flower structure can be seen. The non-uniform cones are observed, and, at the outer edges of the flower, the molten material is seen. In Figure 13d, the flower structure has vanished and transformed into irregular cones with an extended top head on the droplets. The irregular cavities are also prominent at the highest pressure, 50 torr.

4.1.5. Surface Morphology of Cu-Alloy under He Environment without TMF

SEM images of Figure 14a–d reveal the laser-irradiated area of Cu-metal without a magnetic field under He environment at different pressures of 1, 5, 30, and 50 torr. The spherical cones, uplifted droplets, and cavities are dominant features at all pressures. For the lowest pressure of 1 torr, irregular cones with cavities and turbulent melt flow between the cones are seen in Figure 14a. In Figure 14b, a flower-like structure is seen. The spherical-top-headed cones of wider bases are the boundary of the flower structure.

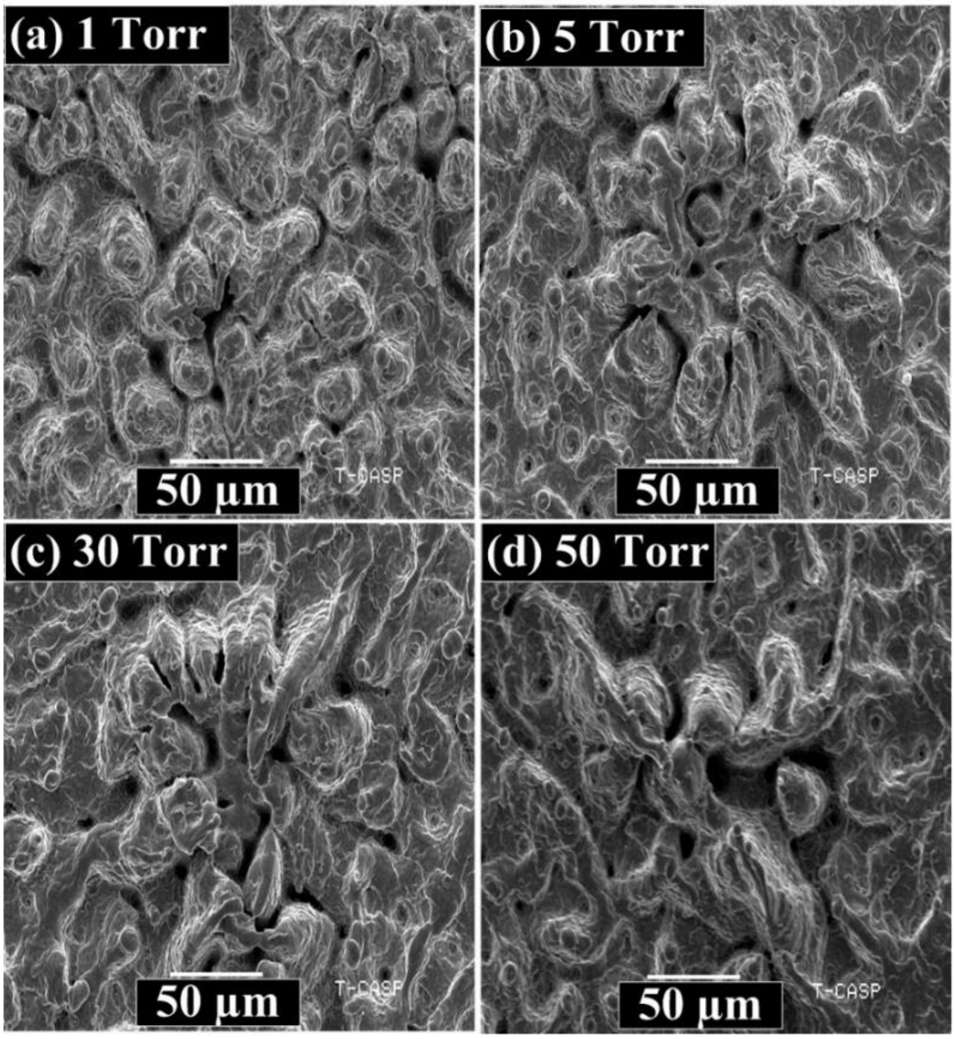

Figure 14. SEM micrographs demonstrating surface morphological changes in a He ambient environment at (**a**) 1 torr, (**b**) 5 torr, (**c**) 30 torr, and (**d**) 50 torr with 3.8 GW/cm^2 laser irradiation in the field-free condition.

At the outer edge of the flower structure, the cones have vanished, and cavities are observed. By increasing the further pressure from 5 torr to 30 and 50 torr, the uniformity of the flower structure decreased. A more irregular and non-uniform flower structure is seen. The density of cones in the flower structure decreased. The cavities' size and the non-uniform melting of the material increased by increasing the pressure.

4.1.6. Surface Morphology of Cu-Alloy under He Environment with TMF

The SEM images in Figure 15a–d represent the surface-modified laser-ablated area of the Cu metal with a magnetic field under He ambient gas environment at different pressures of 1, 5, 30, and 50 torr. The large uplifted spherical cones, cavities, and droplets are main features for all pressures. In Figure 15a, irregular micro-sized cones and non-uniform micro-sized cavities are observed. In Figure 15b, the size of cones is increased, and density decreased at 5 torr pressure. For a pressure of 30 torr, uniform spherical-top-head cones are observed in Figure 15c. The size of the cones increased while density decreased. Large micro-sized cavities between the cones are also observed. For the highest pressure, 50 torr, spherical-top-headed cones have vanished. The non-uniform molten material and turbulent flow are seen. Few cavities are seen with depth.

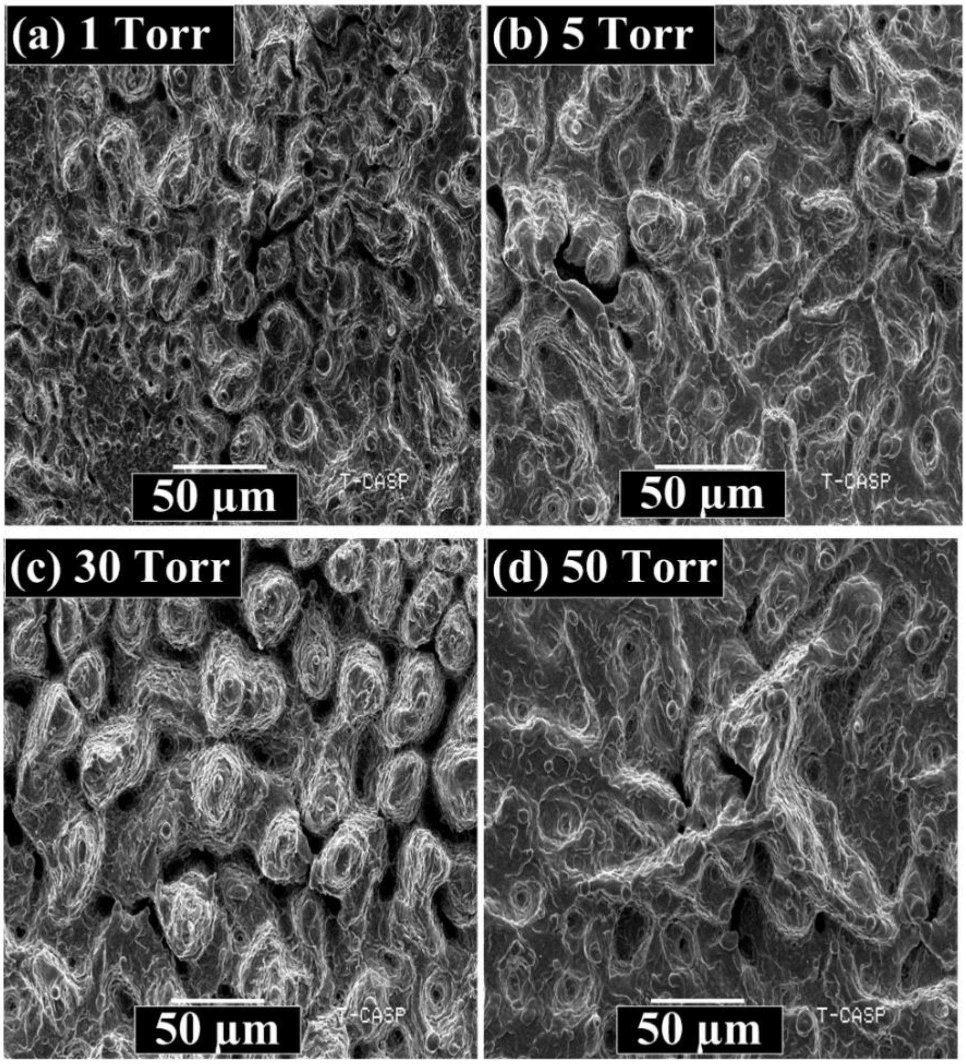

Figure 15. Surface morphological modifications in a He ambient environment at different pressures, (**a**) 1 torr, (**b**) 5 torr, (**c**) 30 torr, and (**d**) 50 torr, with a laser irradiation of 3.8 GW/cm^2 in the TMF.

The applied TMF strongly influences the laser-induced micro/nano structuring. Distinct and regular structures are formed in the case of magnetic field, while diffusive and irregular structures are seen in the absence of a magnetic field. The ambient gas nature and pressure also play a decisive role for uniform and distinct structure formation. The ambient environment properties like E/M ratio, atomic mass, ionization potential, cohesive energy, and thermal conductivity affect the plasma formation on the target surface, which in turn controls the micro and nano structuring on the target material surface. The graphs of Figures 5 and 7 revealed that the electron temperature and electron number density follow the order Ar > He > Ne and reach the maximum at 30 torr pressure. So the applied TMF and ambient environment with suitable pressure where the highest electron temperature and electron number density are achieved are highly desirable for distinct and uniform micro/nano structuring on the target surface.

While comparing the SEM micrographs of Cu-metal without a magnetic field under all environmental gases of Ar, Ne, and He, it has been observed that more diffusive and small-scale structures have been formed in the case of Ar than in Ne and He. The diameter and number density of these cones and cavities are also smallest in the presence of Ar. Overall, the maximum diameter and number density of these cones and cavities have been observed in the presence of He compared to Ar and Ne in the field-free case. The averaged number density of cones and cavities for Ar are (11.21×10^3 cm^{-2} & 11.59×10^3 cm^{-2}), for Ne (21.32 × 10^3 cm^{-2} and 19.47 × 10^3 cm^{-2}), and for He are (22.12 × 10^3 cm^{-2} and 24.40 × 10^3 cm^{-2}), whereas, in the presence of TMF, these conical structures are more distinct and well-defined, with higher maximum number densities in the case of Ne than Ar and He. The averaged number density of cones and cavities for Ar are (8.60 × 10^3 cm^{-2} and 16.86 × 10^3 cm^{-2}), for Ne are (57.61 × 10^3 cm^{-2} and 40.52 × 10^3 cm^{-2}), and for He are (32.40 × 10^3 cm^{-2} and 21.41 × 10^3 cm^{-2}). Averaged cavities and cone densities and their averaged diameter at different pressures of Ar, Ne, and He in the presence and absence of TMF is displayed in Table 5.

Table 5. Averaged cavities and cone densities and their averaged diameter at different pressures of Ar, Ne, and He in the presence and absence of TMF.

Argon							
Without TMF				**With TMF**			
Pressure	**Cavities (10^3)/cm^2**	**Cones (10^3)/cm^2**	**Avg. Cone Dia. (μm)**	**Pressure**	**Cavities (10^3)/cm^2**	**Cones (10^3)/cm^2**	**Avg. Cone Dia. (μm)**
1	21.746	20.757	28.2	1	14.44	8.4	33
5	18.54	12.21	14.7	5	12	3.2	12.1
30	6.1	9.78	17	30	24	13.5	35.4
50	0	2.1	0.9	50	17	9.3	18.7
Average	11.5965	11.21175	15.2	**Average**	16.86	8.6	24.8
Neon							
Without TMF				**With TMF**			
Pressure	**Cavities (10^3)/cm^2**	**Cones (10^3)/cm^2**	**Avg. Cone Dia. (μm)**	**Pressure**	**Cavities (10^3)/cm^2**	**Cones (10^3)/cm^2**	**Avg. Cone Dia. (μm)**
1	28.65	15.287	25.7	1	37.1	80.3	24.2
5	19.94	28	22.7	5	64.9	76.35	24.2
30	10.2	16.56	22	30	31.2	26.87	18.2
50	19.1	25.47	27	50	28.9	46.93	28.75
Average	19.4725	21.32925	24.35	**Average**	40.525	57.6125	23.8375
Helium							
Without TMF				**With TMF**			
Pressure	**Cavities (10^3)/cm^2**	**Cones (10^3)/cm^2**	**Avg. Cone Dia. (μm)**	**Pressure**	**Cavities (10^3)/cm^2**	**Cones (10^3)/cm^2**	**Avg. Cone Dia. (μm)**
1	31.2	31.9	30	1	15.89	28.37	25.3
5	21.2	21.9	29.4	5	12.71	55.6	30.4
30	23.1	22.6	25.7	30	45.94	33.35	35.4
50	22.1	12.1	26.6	50	12.3	12.3	23.8
Average	24.4	22.125	27.925	**Average**	21.71	32.405	28.725

Laser-induced plasma is an excellent tool for developing micro-scale structures that are well-associated with plasma-induced plasma effects and recoil pressure, and it is also one of the greatest sources for thin-layer deposition and the surface structuring of materials in a range of conditions. These structures become purpose-built as their nature, size, and geometry actually influences the surface properties, like optical, electrical, mechanical, and frictional, as well as field emissions, and defines their direct applications in different fields. In present studies, the micro-sized spherical cones are beneficial surface structures that have been considered favorable [43,44,83] for field convergence and as good field and thermionic emitters. Similarly, other structures, such as cavities, pores, and ridges, act as defects and enhance corrosion resistance, the water-repellent property, and strain relief, as well as the adhesive properties [84,85] of a surface, by either reducing or increasing the contact angle between a liquid droplet and the material surface [44]. These features can also enhance the tribological performance of surfaces due to increased surface roughness. In this way, by controlling plasma parameters, it is possible to control surface structuring, coating by plasma, and coating by ion implantation on different materials.

5. Conclusions

In this research, an investigation has been carried out into the impact of a TMF on the pressure dependence of Cu LPP characteristics in three different atmospheres: Ar, Ne, and He. The laser intensity has been kept at a constant level. It was discovered that, regardless of pressure or surrounding conditions, the presence of a magnetic field significantly increases the values of all Cu plasma parameters compared to the field-free scenario. The rise in LPP may be attributed to the synergistic effects of magnetic confinement, Joule's heating, and adiabatic compression. Based on the results, discussion, scanning electron microscopes, and other analysis, the following conclusions may be inferred:

i. Cu plasmas are found to be pressure-dependent in terms of emission intensity, Te, and ne initially; by increasing pressure, all of these parameters increase, and, after reaching their maximums, the electron temperature and electron number density values begin to drop or become saturated as pressure continues to rise. This holds true regardless of the surrounding conditions. Te and ne exhibit the same tendencies in the presence of TMF as they do in the absence of a field over a wide range of environmental variables.

ii. The ambient Ar environment has higher Te and ne spectral intensities than the Ne and He environments under all conditions. Ar has a faster rate of cascade formation and lower thermal conductivity, E/M ratio, and ionization potentials than Ne and He, which explains these results. The confinement of Cu plasma under a 0.6 T TMF is confirmed by analytical assessments, including thermal beta (βt), directional beta (βd), and containment radii (Rs) for different ambient gas pressures.

iii. In the absence of TMF, the formation of less distinct surface structures, such as diffusive cones, cavities, droplets, and non-uniform melting and ridges, is observed on Cu-alloy, whereas, for Cu-alloy in TMF, distinct and well-defined structuring is observed, viz., the large-scale melting, micro-sized spherical cones and cavities, pores, and organized ridges.

iv. Improved Te and ne from a plasma that has been magnetically contained may make it a more useful ion source for ion implantation, thin-film deposition, and coating applications.

Author Contributions: Conceptualization, A.D., S.B., N.A. and A.H.; methodology A.D., S.B., A.H. and N.A.; experimentation, A.D., S.B. and A.H.; validation of data, A.D., S.B., A.H., S.M.A.S., A.A. and N.A.; formal analysis, A.D., S.B., A.H., S.M.A.S.; investigation, A.D., S.B., A.H., S.M.A.S. and N.A.; resources, A.D., S.B., A.H., A.A. and N.A.; writing—original draft preparation, A.D. and S.M.A.S.; writing—review and editing, A.D., S.B., A.H., N.A. and S.M.A.S.; supervision, S.B., A.H. and N.A.; project administration, A.D., S.B., A.H., A.A. and N.A.; All authors have read and agreed to the published version of the manuscript.

Funding: This research received no external funding.

Institutional Review Board Statement: Not applicable.

Informed Consent Statement: Not applicable.

Data Availability Statement: Not applicable.

Conflicts of Interest: The authors declare no conflict of interest.

References

1. Inam, A.; Hegde, M.; Wu, X.; Venkatesan, T.; England, P.; Miceli, P.; Chase, E.; Chang, C.; Tarascon, J.; Wachtman, J. As-deposited high T_c and J_c superconducting thin films made at low temperatures. *Appl. Phys. Lett.* **1988**, *53*, 908–910. [CrossRef]
2. Mao, X.; Russo, R.E.; Liu, H.; Ho, J. As-deposited Sb-doped Bi-Pb-Sr-Ca-Cu-O thin films prepared by pulsed laser deposition. *Appl. Phys. Lett.* **1990**, *57*, 2591–2593. [CrossRef]
3. Sugioka, K.; Toyoda, K. Self-aligned microfabrication of metal-semiconductor contacts by projection-patterned excimer laser doping. *Jpn. J. Appl. Phys.* **1990**, *29*, 2255. [CrossRef]
4. Sternitzke, K.D.; McCreery, R.L. Laser microfabrication and activation of graphite and glassy carbon electrodes. *Anal. Chem.* **1990**, *62*, 1339–1344. [CrossRef]
5. Anderson, R.R.; Parrish, J.A. Selective photothermolysis: Precise microsurgery by selective absorption of pulsed radiation. *Science* **1983**, *220*, 524–527. [CrossRef]
6. Khalid, A.; Bashir, S.; Akram, M.; Hayat, A. Laser-induced breakdown spectroscopy analysis of human deciduous teeth samples. *Lasers Med. Sci.* **2015**, *30*, 2233–2238. [CrossRef]
7. Bulatov, V.; Xu, L.; Schechter, I. Spectroscopic imaging of laser-induced plasma. *Anal. Chem.* **1996**, *68*, 2966–2973. [CrossRef]
8. Amoruso, S.; Bruzzese, R.; Spinelli, N.; Velotta, R. Characterization of laser-ablation plasmas. *J. Phys. B At. Mol. Opt. Phys.* **1999**, *32*, R131. [CrossRef]
9. De Giacomo, A.; Dell'Aglio, M.; Gaudiuso, R.; Amoruso, S.; De Pascale, O. Effects of the background environment on formation, evolution and emission spectra of laser-induced plasmas. *Spectrochim. Acta Part B At. Spectrosc.* **2012**, *78*, 1–19. [CrossRef]
10. Dyer, P.; Issa, A.; Key, P. Dynamics of excimer laser ablation of superconductors in an oxygen environment. *Appl. Phys. Lett.* **1990**, *57*, 186–188. [CrossRef]
11. Harilal, S.S.; Bindhu, C.V.; Tillack, M.S.; Najmabadi, F.; Gaeris, A.C. Internal structure and expansion dynamics of laser ablation plumes into ambient gases. *J. Appl. Phys.* **2003**, *93*, 2380–2388. [CrossRef]
12. Park, S.M.; Moon, J.Y. Laser ablation of graphite in an oxygen jet. *J. Chem. Phys.* **1998**, *109*, 8124–8129. [CrossRef]
13. Mayo, R.; Newman, J.; Sharma, A.; Yamagata, Y.; Narayan, J. Electrostatic measurement of plasma plume characteristics in pulsed laser evaporated carbon. *J. Appl. Phys. A* **1999**, *86*, 2865–2871. [CrossRef]
14. Kim, D.; Park, H.K.; Grigoropoulos, C.P. Interferometric probing of rapid vaporization at a solid–liquid interface induced by pulsed-laser irradiation. *Int. J. Heat Mass Transf.* **2001**, *44*, 3843–3853. [CrossRef]
15. Masubuchi, T.; Tada, T.; Nomura, E.; Hatanaka, K.; Fukumura, H.; Masuhara, H. Laser-induced decomposition and ablation dynamics studied by nanosecond interferometry. 4. A polyimide film. *J. Phys. Chem. A* **2002**, *106*, 2180–2186. [CrossRef]
16. Laube, S.; Voevodin, A. In situ time of flight laser induced florescence spectroscopy of carbon by pulsed laser deposition. *Surf. Coat. Technol.* **1998**, *105*, 125–129. [CrossRef]
17. Glenzer, S.; Fournier, K.; Decker, C.; Hammel, B.; Lee, R.; Lours, L.; MacGowan, B.; Osterheld, A. Accuracy of K-shell spectra modeling in high-density plasmas. *Phys. Rev. E* **2000**, *62*, 2728. [CrossRef]
18. Hayat, A.; Bashir, S.; Rafique, M.S.; Ahmed, R.; Akram, M.; Mahmood, K.; Zaheer, A.; Hussain, T.; Dawood, A. Spatial confinement effects employed by metallic blocker and Ar gas pressures on laser-induced breakdown spectroscopy and surface modifications of laser-irradiated Mg. *Laser Part. Beams* **2017**, *35*, 313–325. [CrossRef]
19. Voevodin, A.; Jones, J.; Zabinski, J. Characterization of ZrO_2/Y_2O_3 laser ablation plasma in vacuum, oxygen, and argon environments. *J. Appl. Phys.* **2000**, *88*, 1088–1096. [CrossRef]
20. Harilal, S. Expansion dynamics of laser ablated carbon plasma plume in helium ambient. *Appl. Surf. Sci.* **2001**, *172*, 103–109. [CrossRef]
21. Cremers, D.A.; Radziemski, L.J. *Handbook of Laser-Induced Breakdown Spectroscopy*; John Wiley & Sons: Hoboken, NJ, USA, 2013.
22. Amin, S.; Bashir, S.; Anjum, S.; Akram, M.; Hayat, A.; Waheed, S.; Iftikhar, H.; Dawood, A.; Mahmood, K. Optical emission spectroscopy of magnetically confined laser induced vanadium pentoxide (V_2O_5) plasma. *Phys. Plasmas* **2017**, *24*, 083112. [CrossRef]
23. Dawood, M.; Margot, J. Effect of ambient gas pressure and nature on the temporal evolution of aluminum laser-induced plasmas. *AIP Adv.* **2014**, *4*, 037111. [CrossRef]
24. Russo, R.; Mao, X.; Liu, C.; Gonzalez, J. Laser assisted plasma spectrochemistry: Laser ablation. *J. Anal. At. Spectrom.* **2004**, *19*, 1084–1089. [CrossRef]
25. Akram, M.; Bashir, S.; Hayat, A.; Mahmood, K.; Ahmad, R.; Rahman, M.K. Effect of laser irradiance on the surface morphology and laser Induced plasma parameters of zinc. *Laser Part. Beams* **2014**, *32*, 119–128. [CrossRef]
26. Akram, M.; Bashir, S.; Rafique, M.S.; Hayat, A.; Mahmood, K. Laser induced surface morphology of molybdenum correlated with breakdown spectroscopy. *Plasma Chem. Plasma Process.* **2017**, *37*, 287–304. [CrossRef]
27. Arshad, A.; Bashir, S.; Hayat, A.; Akram, M.; Khalid, A.; Yaseen, N.; Ahmad, Q.S. Effect of magnetic field on laser-induced breakdown spectroscopy of graphite plasma. *Appl. Phys. B* **2016**, *122*, 63. [CrossRef]
28. Neogi, A.; Thareja, R. Dynamics of laser produced carbon plasma expanding in a nonuniform magnetic field. *J. Appl. Phys.* **1999**, *85*, 1131–1136. [CrossRef]
29. Hussain, A.; Qi, L.; Zuoqiang, H.; Xun, G.; Jingquan, L. The Effect of an External Magnetic Field on the Plume Expansion Dynamics of Laser-Induced Aluminum Plasma. *Plasma Sci. Technol.* **2015**, *17*, 693. [CrossRef]
30. Winske, D. Development of flute modes on expanding plasma clouds. *Phys. Fluids* **1989**, *1*, 1900–1910. [CrossRef]

31. Neogi, A.; Thareja, R.K. Laser-produced carbon plasma expanding in vacuum, low pressure ambient gas and nonuniform magnetic field. *Phys. Plasmas* **1999**, *6*, 365–371. [CrossRef]
32. Gekelman, W.; Van Zeeland, M.; Vincena, S.; Pribyl, P. Laboratory experiments on Alfvén waves caused by rapidly expanding plasmas and their relationship to space phenomena. *J. Geophys. Res. Space Phys.* **2003**, *108*, 1281. [CrossRef]
33. Kawasaki, H.; Doi, K.; Hiraishi, S.; Suda, Y. Effects of cross-magnetic field on thin film preparation by pulsed Nd/YAG laser deposition. *Thin Solid Film.* **2000**, *374*, 278–281. [CrossRef]
34. Harilal, S.; O'Shay, B.; Tillack, M.S. Debris mitigation in a laser-produced tin plume using a magnetic field. *J. Appl. Phys.* **2005**, *98*, 036102. [CrossRef]
35. Cowpe, J.; Pilkington, R.; Astin, J.; Hill, A. The effect of ambient pressure on laser-induced silicon plasma temperature, density and morphology. *J. Phys. D Appl. Phys* **2009**, *42*, 165202. [CrossRef]
36. Patel, D.; Pandey, P.K.; Thareja, R.K. Brass plasmoid in external magnetic field at different air pressures. *Phys. Plasmas* **2013**, *20*, 103503. [CrossRef]
37. Raju, M.S.; Singh, R.; Gopinath, P.; Kumar, A. Influence of magnetic field on laser-produced barium plasmas: Spectral and dynamic behaviour of neutral and ionic species. *J. Appl. Phys.* **2014**, *116*, 153301. [CrossRef]
38. Rai, V.; Singh, J.P. Effect of laser intensity and dynamics of plasma on laser induced breakdown spectroscopy. *arXiv* **2014**, arXiv:1406.7703.
39. Corsi, M.; Cristoforetti, G.; Hidalgo, M.; Iriarte, D.; Legnaioli, S.; Palleschi, V.; Salvetti, A.; Tognoni, E. Effect of laser-induced crater depth in laser-induced breakdown spectroscopy emission features. *Appl. Spect.* **2005**, *59*, 853–860. [CrossRef]
40. Rai, V.N.; Zhang, H.; Yueh, F.Y.; Singh, J.P.; Kumar, A. Effect of steady magnetic field on laser-induced breakdown spectroscopy. *Appl. Opt.* **2003**, *42*, 3662–3669. [CrossRef]
41. Hussain, A.; Asghar, H.; Iqbal, T.; Ishfaq, M.; Shahbaz, R.M.; Riaz, Q. Improving the spectral intensity of aluminum plasma by applied-magnetic field in laser-induced breakdown spectroscopy. *Optik* **2021**, *251*, 168220. [CrossRef]
42. Liu, P.; Hai, R.; Wu, D.; Xiao, Q.; Sun, L.; Ding, H. The enhanced effect of optical emission from laser induced breakdown spectroscopy of an Al-Li alloy in the presence of magnetic field confinement. *Plasma Sci. Technol.* **2015**, *17*, 687. [CrossRef]
43. Wang, T.; Yasuda, K.; Nishikawa, H. Fabrication of micron-sized protrusions on metal surface for metal/polymer easy-disassembly joining by selective laser melting technology. *Mater. Des.* **2022**, *220*, 110873. [CrossRef]
44. Min, J.; Wan, H.; Carlson, B.E.; Lin, J.; Sun, C. Application of laser ablation in adhesive bonding of metallic materials: A review. *Opt. Laser Technol.* **2020**, *128*, 106188. [CrossRef]
45. Singh, K.S.; Sharma, A.K. Time-integrated optical emission studies on laser-produced copper plasma in the presence of magnetic field in air ambient at atmospheric pressure. *Appl. Phys. A* **2017**, *123*, 325. [CrossRef]
46. WikiPedia. Available online: https://en.wikipedia.org/wiki/Gilding_metal (accessed on 10 December 2022).
47. Demtröder, W. *Laser Spectroscopy: Basic Concepts and Instrumentation*; Springer Science & Business Media: Berlin/Heidelberg, Germany, 2013.
48. List, I.A. Atomic Line List v3.00b4. Available online: http://www.pa.uky.edu/~{}peter/newpage/ (accessed on 18 August 2021).
49. Reader, J.; Corliss, C.H.; Wiese, W.; Martin, G. *Wavelengths and Transition Probabilities for Atoms and Atomic Ions: Part 1. Wavelengths, Part 2. Transition Probabilities*; NSRDS-NBS.; National Institute of Standards and Technology: Gaithersburg, MD, USA, 1980; Volume 68, p. 409.
50. Singh, K.S.; Sharma, A.K. Multi-structured temporal behavior of neutral copper transitions in laser-produced plasma in the presence of variable transverse static magnetic field. *Phys. Plasmas* **2016**, *23*, 013304. [CrossRef]
51. Li, Y.; Hu, C.; Zhang, H.; Jiang, Z.; Li, Z. Optical emission enhancement of laser-produced copper plasma under a steady magnetic field. *App. Opt.* **2009**, *48*, B105–B110. [CrossRef]
52. Cheng, L.; Xun, G.; Qi, L.; Chao, S.; Jingquan, L. Spectral enhancement of laser-induced breakdown spectroscopy in external magnetic field. *Plasma Sci. Technol.* **2015**, *17*, 919–922.
53. Harilal, S.; Tillack, M.; O'shay, B.; Bindhu, C.; Najmabadi, F. Confinement and dynamics of laser-produced plasma expanding across a transverse magnetic field. *Phys. Rev. E* **2004**, *69*, 026413. [CrossRef]
54. Iftikhar, H.; Bashir, S.; Dawood, A.; Akram, M.; Hayat, A.; Mahmood, K.; Zaheer, A.; Amin, S.; Murtaza, F. Magnetic field effect on laser-induced breakdown spectroscopy and surface modifications of germanium at various fluences. *Laser Part. Beams* **2017**, *35*, 159–169. [CrossRef]
55. Joshi, H.; Kumar, A.; Singh, R.; Prahlad, V. Effect of a transverse magnetic field on the plume emission in laser-produced plasma: An atomic analysis. *Spectrochim. Acta B* **2010**, *65*, 415–419. [CrossRef]
56. Kim, T.H.; Nam, S.H.; Park, H.S.; Song, J.K.; Park, S.M. Effects of transverse magnetic field on a laser-produced Zn plasma plume and ZnO films grown by pulsed laser deposition. *Appl. Surf. Sci* **2007**, *253*, 8054–8058. [CrossRef]
57. Shen, X.; Lu, Y.; Gebre, T.; Ling, H.; Han, Y. Optical emission in magnetically confined laser-induced breakdown spectroscopy. *J. Appl Phys.* **2006**, *100*, 053303. [CrossRef]
58. Harilal, S.; Sizyuk, T.; Hassanein, A.; Campos, D.; Hough, P.; Sizyuk, V. The effect of excitation wavelength on dynamics of laser-produced tin plasma. *J. Appl. Phys.* **2011**, *109*, 063306. [CrossRef]
59. Nakimana, A.; Tao, H.; Camino, A.; Gao, X.; Hao, Z.; Lin, J. Effect of ambient pressure on femtosecond laserinduced breakdown spectroscopy of Al in Argon. In Proceedings of the International Conference on Optoelectronics and Microelectronics (ICOM), Changchun, Jilin, 23–25 August 2012; pp. 146–150.

60. Luo, W.; Zhao, X.; Sun, Q.; Gao, C.; Tang, J.; Wang, H.; Zhao, W. Characteristics of the aluminum alloy plasma produced by a 1064 nm Nd: YAG laser with different irradiances. *Pramana* **2010**, *74*, 945–959. [CrossRef]
61. Radziemski, L.J.; Cremers, D.A. *Laser-Induced Plasmas and Applications*; CRC Press: Boca Raton, FL, USA, 1989.
62. Farid, N.; Bashir, S.; Mehmood, K. Effect of ambient gas conditions on laser-induced copper plasma and surface morphology. *Phys. Scr.* **2012**, *85*, 015702. [CrossRef]
63. Farid, N.; Harilal, S.S.; Ding, H.; Hassanein, A. Emission features and expansion dynamics of nanosecond laser ablation plumes at different ambient pressures. *J. Appl. Phys.* **2014**, *115*, 033107. [CrossRef]
64. Harilal, S.S.; Bindhu, C.V.; Nampoori, V.P.N.; Vallabhan, C.P.G. Influence of ambient gas on the temperature and density of laser produced carbon plasma. *Appl. Phys. Lett.* **1998**, *72*, 167–169. [CrossRef]
65. Knight, A.K.; Scherbarth, N.L.; Cremers, D.A.; Ferris, M. Characterization of laser-induced breakdown spectroscopy (LIBS) for application to space exploration. *Appl. Spectrosc.* **2000**, *54*, 331–340. [CrossRef]
66. Iida, Y. Effects of atmosphere on laser vaporization and excitation processes of solid samples. *Spectrochim. Acta B* **1990**, *45*, 1353–1367. [CrossRef]
67. Effenberger, A.J.; Scott, J.R. Effect of atmospheric conditions on LIBS spectra. *Sensors* **2010**, *10*, 4907–4925. [CrossRef]
68. Boyd, T.J.M.; Sanderson, J.J. *The Physics of Plasmas*; Cambridge University Press: Cambridge, UK, 2003.
69. Peyser, T.; Manka, C.; Ripin, B.; Ganguli, G. Electron–ion hybrid instability in laser-produced plasma expansions across magnetic fields. *Phys. Fluids B* **1992**, *4*, 2448–2458. [CrossRef]
70. Bleiner, D.; Bogaerts, A. Multiplicity and contiguity of ablation mechanisms in laser-assisted analytical micro-sampling. *Spectrochim. Acta B* **2006**, *61*, 421–432. [CrossRef]
71. Zuhlke, C.A.; Anderson, T.P.; Alexander, D.R. Formation of multiscale surface structures on nickel via above surface growth and below surface growth mechanisms using femtosecond laser pulses. *Opt. Express* **2013**, *21*, 8460–8473. [CrossRef] [PubMed]
72. Bashir, S.; Khurshid, S.; Akram, M.; Ali, N.; Ahmad, S.; Yousaf, D. Pulsed laser ablation of Ni in vacuum and N_2 atmosphere at various fluences. *Quantum Electron.* **2015**, *45*, 640–647. [CrossRef]
73. Mansour, N.; Jamshidi-Ghaleh, K.; Ashkenasi, D. Formation of conical microstructures of silicon with picosecond laser pulses in air. *JLMN* **2006**, *1*, 12–16. [CrossRef]
74. Sarfraz, S.M.A.; Bashir, S.; Mahmood, K.; Khaliq, A.; Rizvi, R. Fluence-dependent sputtering yield measurement, surface morphology, crater depth, and hardness of laser-irradiated Zr in N_2 and Ne environments. *J. Opt. Soc. Am. B* **2019**, *36*, 1945–1957. [CrossRef]
75. Körner, C.; Mayerhofer, R.; Hartmann, M.; Bergmann, H.W. Physical and material aspects in using visible laser pulses of nanosecond duration for ablation. *J. Appl. Phys. A* **1996**, *63*, 123–131. [CrossRef]
76. Tokarev, V. Viscous liquid expulsion in nanosecond UV laser ablation: From "clean" ablation to nanostructures. *Laser Phys.* **2006**, *16*, 1291–1307. [CrossRef]
77. Lappalainen, J.; Frantti, J.; Lantto, V. Particulate formation in PZT thin films during pulsed laser ablation deposition. *Korean Phys. Soc.* **1998**, *32*, S1183–S1186.
78. Aristov, Y.I.; Tokarev, M.M.; Freni, A.; Glaznev, I.S.; Restuccia, G. Kinetics of water adsorption on silica Fuji Davison RD. *Microporous Mesoporous Mater.* **2006**, *96*, 65–71. [CrossRef]
79. Yousaf, D.; Bashir, S.; Akram, M.; Kalsoom, U.-I.; Ali, N. Laser irradiation effects on the surface, structural and mechanical properties of Al–Cu alloy 2024. *Radiat. Eff. Defects Solids* **2014**, *169*, 144–156. [CrossRef]
80. Dauscher, A.; Feregotto, V.; Cordier, P.; Thomy, A. Laser induced periodic surface structures on iron. *Appl. Surf. Sci.* **1996**, *96*, 410–414. [CrossRef]
81. Barmina, E.V.; Barberoglu, M.; Zorba, V.; Simakin, A.V.; Stratakis, E.; Fotakis, K.; Shafeev, G.A. Surface nanotexturing of tantalum by laser ablation in water. *Quantum Electron.* **2009**, *39*, 89. [CrossRef]
82. Ko, S.H.; Pan, H.; Hwang, D.J.; Chung, J.; Ryu, S.; Grigoropoulos, C.P.; Poulikakos, D. High resolution selective multilayer laser processing by nanosecond laser ablation of metal nanoparticle films. *J. Appl. Phys.* **2007**, *102*, 093102. [CrossRef]
83. Obilor, A.F.; Pacella, M.; Wilson, A.; Silberschmidt, V.V. Micro-texturing of polymer surfaces using lasers: A review. *J. Adv. Manuf. Technol.* **2022**, *120*, 103–135. [CrossRef]
84. Tofil, S.; Barbucha, R.; Kocik, M.; Kozera, R.; Tański, M.; Arivazhagan, N.; Yao, J.; Zrak, A. Adhesive Joints with Laser Shaped Surface Microstructures. *Materials* **2021**, *14*, 7548. [CrossRef]
85. Rudawska, A. Adhesive properties of metals and metal alloys. In *Surface Energy*; Aliofkhazraei, M., Ed.; InTech: Rijeka, Croatia, 2015; pp. 85–121.